Time histories of tensile force in geogrid arranged in two full-scale high walls

W. Kongkitkul[1], F. Tatsuoka[2], D. Hirakawa[3], T. Sugimoto[4], S. Kawahata[5] and M. Ito[6]

[1]*Lecturer, Department of Civil Engineering, King Mongkut's University of Technology Thonburi, 126 Pracha u-tid Road, Bangmod, Toongkru, Bangkok, 10140, Thailand, Telephone: +66 2 470 9144, Telefax: +66 2 427 9063, E-mail: warat.kon@kmutt.ac.th*
[2]*Professor, Department of Civil Engineering, Tokyo University of Science, 2641 Yamazaki, Noda, Chiba, 278–8510, Japan, Telephone: +81 4 7122 9819, Telefax: +81 4 7123 9766, E-mail: tatsuoka@rs.noda.tus.ac.jp*
[3]*Assistant Professor, Department of Civil and Environmental Engineering, National Defense Academy, 1–10–20 Hashirimizu, Yokosuka, 239–8686, Japan, Telephone: +81 4 6841 3810 (ext. 3514), Telefax: +81 4 6844 5913, E-mail: hirakawa@nda.ac.jp*
[4]*Engineer, Shizuoka Prefecture, 9–6 Otemachi, Aoi-ku, Shizuoka, Japan, 420–8601, Telephone: +81 54 221 3043, Telefax: +81 54 221 3564, E-mail: toshihiko1_sugimoto@pref.shizuoka.lg.jp*
[5]*Consulting engineer, Nippon-koei Co., Ltd., Nagoya Branch, 2–17–14 Higashisakura, Higashi-ku, Nagoya, Aichi, Japan, 461–0005, Telephone: +81 52 559 7301, Telefax: +81 52 939 3472, E-mail: a5054@n-koei.co.jp*
[6]*Engineer, Maeda-Kosen Co., Ltd., Nihon-bashi Building 5F, Hisamatsuo-cho, Nihonbashi, Chuo-ku, Tokyo, Japan, 103–0005, Telephone: +81 3 3663 7828, Telefax: +81 3 3663 9930, E-mail: m_ito@mdk.co.jp*

Received 27 July 2009, revised 17 November 2009, accepted 18 November 2009

ABSTRACT: Two tall geosynthetic-reinforced soil (GRS) walls, one 16.7 m high supporting a sloped embankment, and the other 21.1 m high with a level backfill, were constructed to support the taxi way of Mt. Fuji Shizuoka Airport, Shizuoka Prefecture, Japan, which was opened to service in June 2009. As only limited residual deformation during service is allowed and high stability is required, the backfill was a well-graded gravelly soil, which was well compacted at controlled water content and reinforced with geogrid reinforcement. In the respective walls, three representative geogrid layers were fitted with a number of electric-resistance strain gauges to monitor the geogrid tensile strains during and after construction to ensure high stability and sufficient serviceability. After the wall construction had been completed, the geogrid strains were either only increasing at a very low rate, or had stopped increasing, or had started decreasing. A series of in-air tensile loading tests were performed on different geogrid types used for the wall construction to evaluate their elasto-viscoplastic properties. The time histories of tensile force in the geogrid layers were estimated from the measured time histories of the geogrid strains based on a non-linear three-component rheology model using the model parameters determined by the in-air tensile loading tests. After the end of wall construction, the estimated geogrid tensile force was either increasing at a very low rate or was decreasing with time. Even at the locations where it tended to increase with time, the estimated geogrid tensile force never increased greatly by the end of a typical design life (i.e. 50 years) from the value at the end of wall construction. As the estimated maximum geogrid force at the end of the design lifetime is substantially lower than the respective design tensile rupture strengths, it is estimated that creep rupture failure of the geogrid is utterly unlikely. The analysis suggests that these estimates are also relevant when the lifetime is 100 years. The framework to estimate the time histories of reinforcement force from the time histories of measured reinforcement strains used in this study can be applied to other similar cases.

KEYWORDS: Geosynthetics, Creep, Elasto-viscoplastic property, Geogrid, Reinforced soil walls, Full-scale behaviour, Rate effect

REFERENCE: Kongkitkul, W., Tatsuoka, F., Hirakawa, D., Sugimoto, T., Kawahata, S. & Ito, M. (2010). Time histories of tensile force in geogrid arranged in two full-scale high walls. *Geosynthetics International*, **17**, No. 1, 12–33. [doi: 10.1680/gein.2010.17.1.12]

1. INTRODUCTION

A number of permanent geosynthetic-reinforced soil (GRS) structures, including retaining walls (RWs), bridge abutments, steep-sloped embankments, dykes and earth-fill dams and fills supporting shallow foundations, have been constructed. The popularity of this technology is due mainly to cost-effectiveness resulting from rapid construction, a relative small construction space requirement, the use of a substantially smaller amount of concrete and steel, and high post-construction performance including high seismic stability (e.g., Tatsuoka *et al.* 1997, 1998, 2007; Koseki *et al.* 2006; Latha and Krishna 2008). Despite the use of so-called extensible reinforcement (i.e., polymeric geosynthetic reinforcement), as far as the authors know, there is no reported case of ordinary permanent GRS structures that have deformed excessively due to too much creep deformation, or have collapsed due to creep having caused rupture of the polymeric geosynthetic reinforcement. This may be due mainly to the following two causes. First, the actual safety factor against failure of a given GRS structure under static loading conditions is considerably higher than unity when adequately designed against seismic loads. The safety margin under static loading conditions becomes larger as the design seismic load becomes greater. Second, there are several hidden conservatisms in the design, including the following situations.

1. The shear strength of the backfill used in the design may be considerably lower than the true peak shear strength, in particular when good backfill is well-compacted (as in the cases of ordinary permanent important GRS structures) (e.g. Tatsuoka 2008, 2009).
2. The positive effects of suction in unsaturated backfill, which could be significant during dry seasons or even during wet seasons when an effective drainage system is provided, are usually ignored in design to prepare for the worst rainfall condition anticipated during a given lifetime where the positive effects of suction may be lost.
3. The tensile strength of polymeric geosynthetic reinforcement used in design is obtained by significantly reducing the strength measured in fast tensile tests on the new products using a relatively large creep reduction factor. This procedure is adopted to remove the possibility of creep rupture failure by considering that polymeric geosynthetic reinforcement generally exhibits highly rate-dependent behaviour due to its viscous properties (e.g. Hirakawa *et al.* 2003; Kongkitkul *et al.* 2004, 2007a). In this respect, it seems that the current design concept is rather conservative for ordinary, properly designed and constructed GRS walls (e.g. Tatsuoka *et al.* 2004, 2006; Tatsuoka 2008). The creep reduction factor is applied after the strength has been reduced by applying not only an installation damage factor but also a material degradation factor. In particular, it is assumed that geosynthetic reinforcement only starts exhibiting creep deformation after the full negative effects of material degradation (chemical and/or biological) have occurred by the end of the prescribed lifetime. Kongkitkul *et al.* (2007d) showed that this is a conservative assumption. In reality, creep deformation and degradation take place simultaneously. As a result of these procedures, the design tensile rupture strength becomes significantly lower than the initial strength determined by fast tensile loading tests on the new products. Having included all the factors for conservation identifed above, it is usually very unlikely that any creep failure of the geosynthetic reinforcement will take place in a given GRS structure at the actual working load by the end of the prescribed lifetime.

With respect to factor 3 above, it is assumed in the current design that the tensile force activated in the geosynthetic reinforcement is kept constant throughout the prescribed lifetime of a given GRS structure. However, the backfill is also an elasto-viscoplastic material, similar to the polymeric geosynthetic reinforcement. Therefore, the backfill may exhibit creep deformation in the longitudinal direction of reinforcement, either in compression caused by confining pressure activated by the tensile force in the reinforcement, or in extension caused by unstable deformation of the wall, or both. Kongkitkul *et al.* (2007b, c, e; 2008a) performed a series of plane strain compression (PSC) tests on specimens comprising geosynthetic-reinforced sand to investigate the interaction mechanism between sand and geosynthetic reinforcement. To this end, the time history of the tensile force activated in the polymeric geosynthetic reinforcement was evaluated from measured time histories of geosynthetic reinforcement strain. They showed that, under a constant working load at the boundary of the specimen that is sufficiently lower than the collapsed load, the tensile force of geosynthetic reinforcement may decrease with time. If this phenomenon takes place with a given full-scale GRS structure, this factor becomes another hidden conservatism in the design of the GRS structure.

Mt. Fuji Shizuoka Airport in Shizuoka Prefecture in Japan was opened to the public in June 2009. For this airport, two high geosynthetic-reinforced soil (GRS) walls (16.7 and 21.1 m high) were constructed (Figure 1; Fujinami *et al.* 2007, 2009; Fujita *et al.* 2007; Takagi *et al.*, 2007). These two high GRS walls were constructed in two valleys to preserve the natural environment, which consisted of forests and swamp areas in front of the walls and which would be buried in the backfill if gentle-sloped embankments were constructed. Continuous monitoring of the tensile strains in three representative geogrid layers in the respective walls during and after construction provided an excellent opportunity to determine whether the current design method is very conservative with respect to the tensile force activated in the geogrid, whether excessive creep deformation and creep rupture of the geogrid is or is not likely to take place, and more specifically whether the

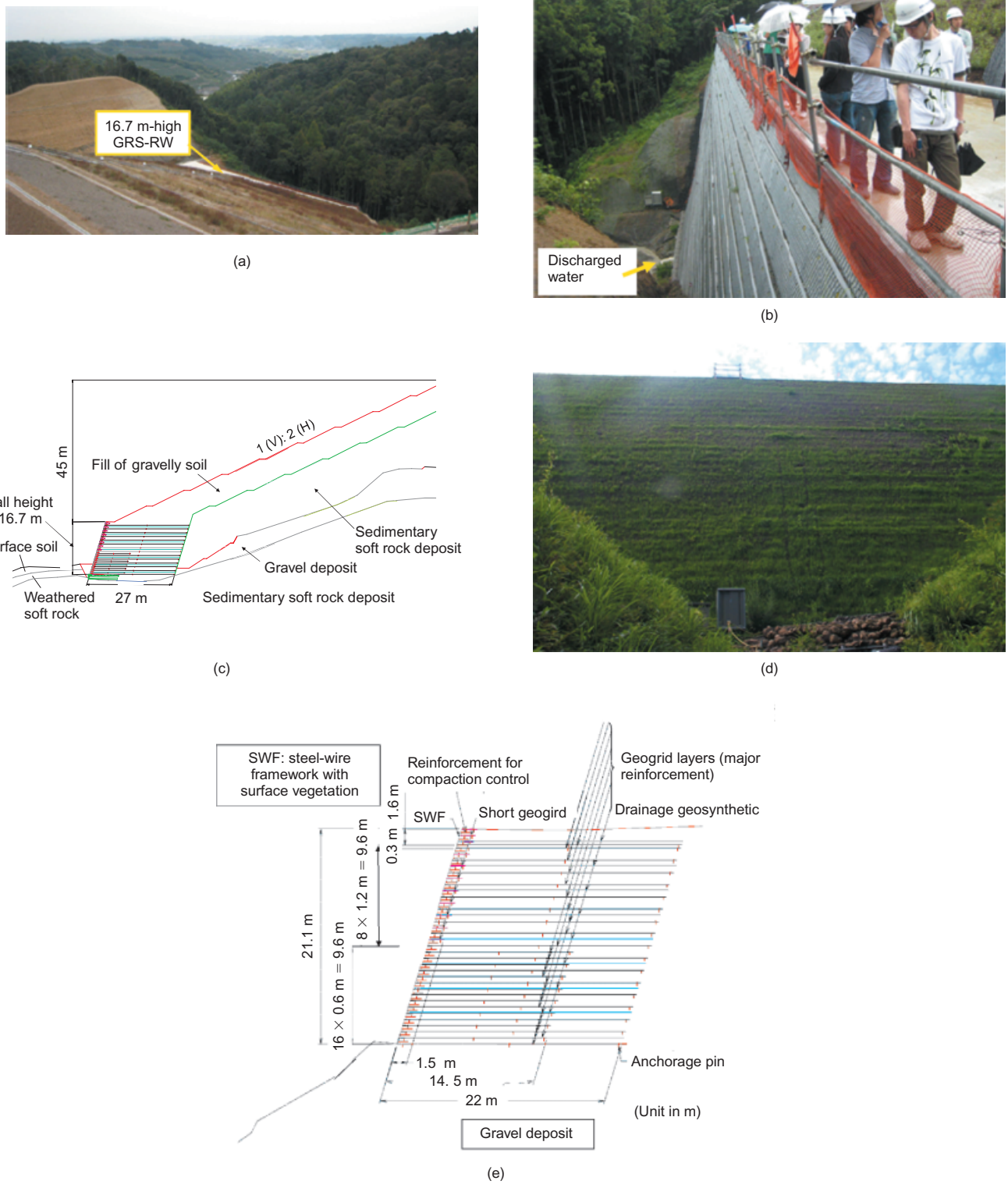

Figure 1. Two high GRS walls constructed for Mt. Fuji Shizuoka Airport: (a) back view; (b) a view from the crest during rainfall, before vegetation of the wall face; (c) cross-section of the wall in valley 1; (d) front view; and (e) cross-section of the wall in valley 2 (modified from Fujita *et al.* 2008)

tensile force mobilised in the geogrid is kept constant after the end of wall construction in field full-scale cases.

In this study, the time histories of the tensile force activated in six (in total) geogrid layers in these two GRS walls were evaluated from the measured time histories of the geogrid tensile strain. The time histories of the geogrid force by the end of a lifetime equal to 50 years, which is typical of ordinary civil engineering structures, were then predicted by extrapolating the time histories of the geogrid tensile strains that were measured up to the current stage

(when this paper was prepared). These analyses were performed based on a non-linear three-component elasto-viscoplastic model that has been validated as being able to properly describe the rate-dependent load–strain behaviour of a number of different types of polymeric geosynthetic reinforcement (e.g. Hirakawa *et al.* 2003; Kongkitkul *et al.*, 2004, 2007a, d; Kongkitkul and Tatsuoka 2007). The analyses indicated that, even at the most severely loaded locations of the geogrid layers among those analysed, the tensile force had increased only slightly from the initial value at the end of wall construction. The estimated maximum geogrid tensile force was significantly lower than the design tensile strength (i.e. the value after having been reduced from the fast loading strength of new products by using a creep reduction factor). At the other locations where the tensile strains were kept nearly constant or even noticeably decreased with time, even the tensile force had decreased with time, or the geogrid was exhibiting even unloading. It was estimated that the possibility of excessive tensile deformation and creep rupture of the geogrid by the end of the typical lifetime (50 years) was very low for these two walls. Part of the analyses presented in this paper has been reported by Kongkitkul *et al.* (2008b) and Tatsuoka (2008).

2. CONSTRUCTION AND PERFORMANCE OF THE WALLS

Figures 1(c) and (e) show the cross-sections of the two walls. As the walls support the west side of the taxi way of the airport, it is necessary to ensure small residual displacements at the crest of the walls during service. A sufficiently high stability during severe earthquakes and heavy rainfall is another important design factor. Moreover, to maintain the natural environment in front of the walls which was to be preserved by the construction of the walls, planting of vegetation on the wall faces was required. To satisfy these requirements, well-graded gravelly soil, which was retrieved from a nearby ancient river bed (Figure 2) and consisted of round gravelly particles and sub-angular smaller particles, was selected for use as the backfill. Figure 3(a) shows representative compaction

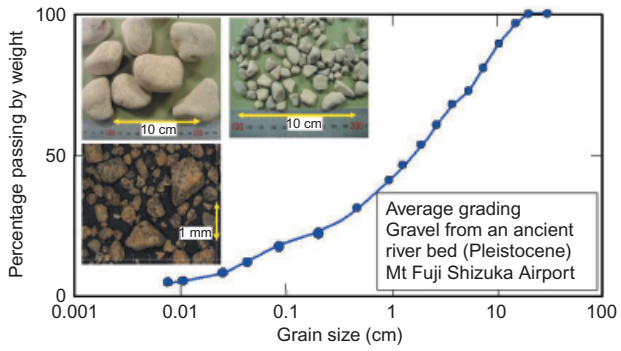

Figure 2 Average grading curve and particle pictures of the backfill used to construct the two GRS walls of Mt. Fuji Shizuoka Airport (modified from Fujita *et al.* 2007; Takagi *et al.*, 2007)

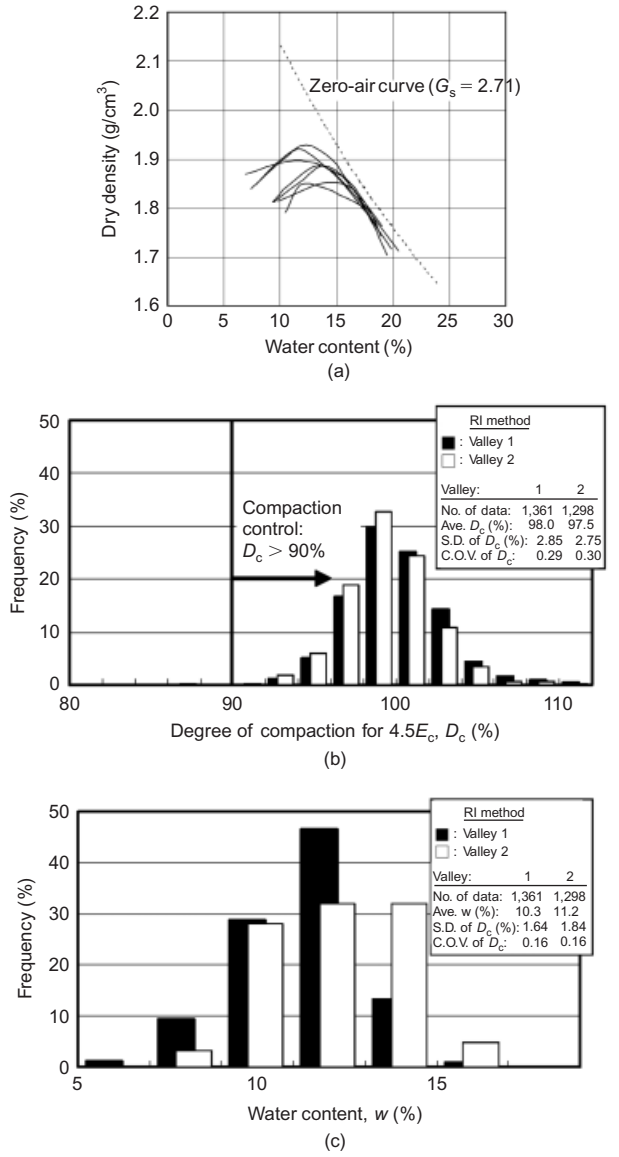

Figure 3. (a) Typical compaction curves (modified Proctor) of the backfill used to construct two GRS walls for Mt. Fuji Shizuoka Airport; (b) distributions of measured degrees of compaction of the backfill; and (c) distributions of water content during compaction, RI (radio isotope) method (modified from Fujinami *et al.* 2007, 2009; Fujita *et al.* 2007, 2008; Takagi *et al.*, 2007)

curves obtained by compaction tests using compaction energy that was 4.5 times higher than the standard Proctor (i.e., the modified Proctor) performed for field compaction control. The backfill in the two walls was compacted to lifts with a thickness of 30 cm, which is a half or one-quarter of the basic vertical spacing between the major geogrid reinforcement layers (60 or 120 cm), by using 10 tonf-class vibratory compactors. Figure 3(b) shows the distributions of the degree of compaction of the backfill (i.e. the ratio of the field dry density measured by the radio isotope method for every area of 1000 m^2 to the respective values of the maximum dry density by the modified Proctor; Figure 3(a)). As seen from Figure 3(b), the backfill was compacted very well to an average degree of compaction greater than 95%. The water content during

compaction was controlled to be close to the optimum (Figure 3(c)). Effective drainage systems were arranged inside and at the base of the backfill in the two walls. To acieve this, a network of perforated drainage pipes, covered with a non-woven geotextile, were buried along the boundary between the fill (i.e., the backfill of the walls and the embankments behind) and the existing ground. In addition, horizontal drainage geosynthetic strips (5 mm thick × 300 mm wide) were arranged inside the embankment per 3 m^2 of wall face area (Figure 1(e); Fujinami *et al.* 2009). A zone of crushed stone gravel immediately behind the wall face was also arranged to smoothly drain water collected by the horizontal drainage strips as well as water from the wall backfill and embankment. At the centre and the bottom of the wall face, where the water is finally discharged from the wall, mat gabions and crushed stone gabions were arranged to prevent scouring. It may be seen in Figure 1(b) that water is being discharged from the outlet of the central main drainage pipe arranged along the centre-line of the wall during rainfall.

The geogrid made of Aramid fibre coated with HDPE was used to reinforce the backfill. Figures 4(a) and (b) show the tensile loading test on one product of this type of geogrid performed by Hirakawa *et al.* (2003) and Figure 4(c) shows a typical test result from which the viscous property was evaluated. In addition, Figure 4(d) shows the simulated result of Figure 4(c) by a non-linear three-component model (explained later). Figures 1(c) and (e) and Figures 5(a) and (b) show the details of the arrangements of geogrid reinforcement in the two walls. Seven different types having different densities of Aramid fibre and therefore different design rupture strengths T_A ranging from 20 to 87 kN/m were used. Generally, stronger geogrids were arranged at lower places in the walls. The properties of the three representative geogrid types on which electric-resistance strain gauges were attached in the two walls are listed in Table 1. For a length of 1.5 m from the wall face, relatively weak secondary geogrid layers were additionally arranged at the mid-height between the upper and lower adjacent major geogrid layers to enhance better compaction of the backfill and to increase the stability of the backfill zone immediately behind the wall face. The wall face was protected by using 60 cm-high L-shaped galvanized expanded-metal mesh facing units (Figure 6). The major

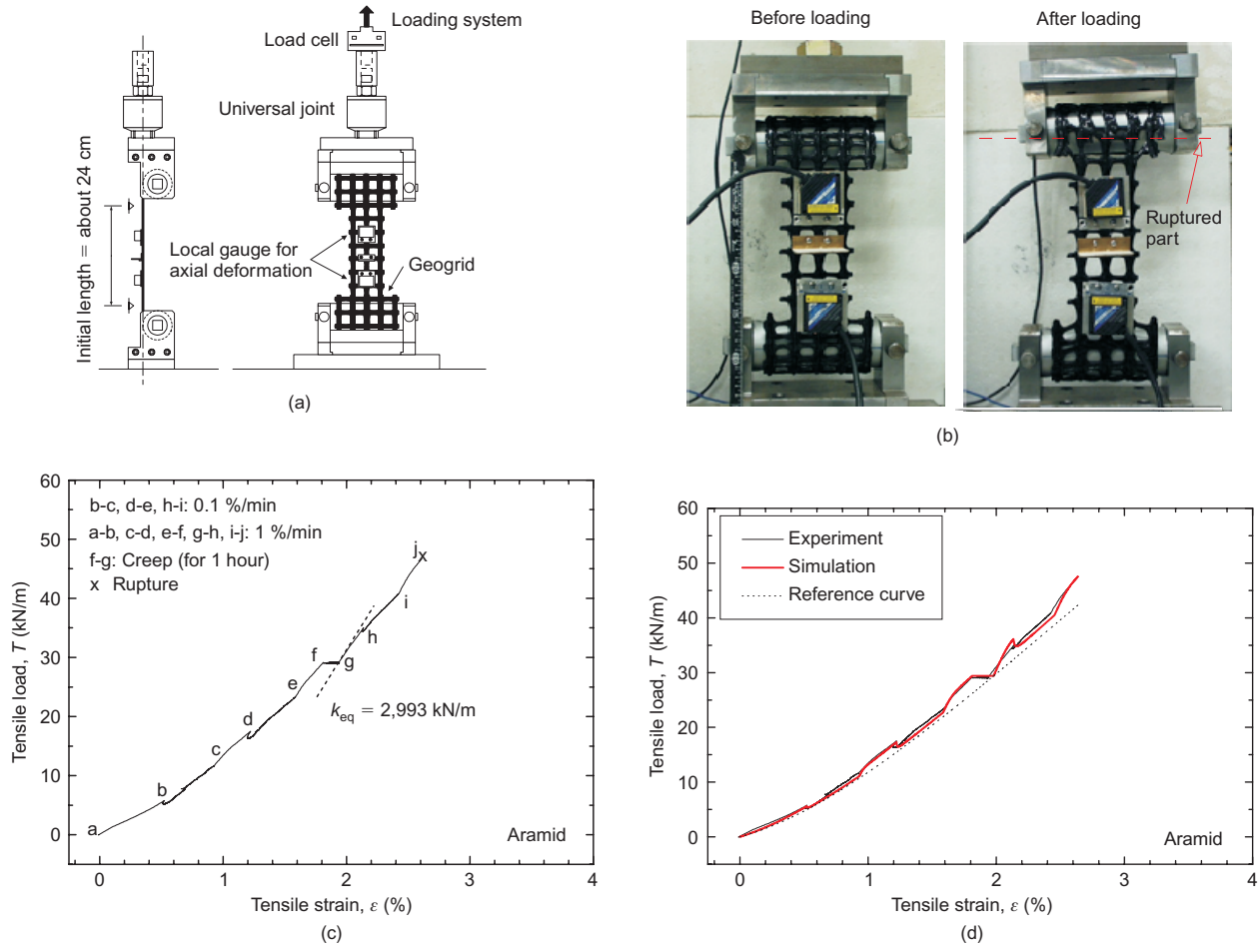

Figure 4. (a) Tensile loading device with a geogrid specimen of Aramid fibre (the average rupture strength from many tests on new product at a strain rate of 1 %/min = 56 kN/m); (b) a typical ruptured specimen; (c) load–strain curve in which the strain rate was stepwise changed and sustained loading test was performed (note: the rupture strength in this test is slightly lower than 56 kN/m due to a variance of product, k_{eq}: elastic stiffness); and (d) simulation by the three-component model (modified from Hirakawa *et al.* 2003)

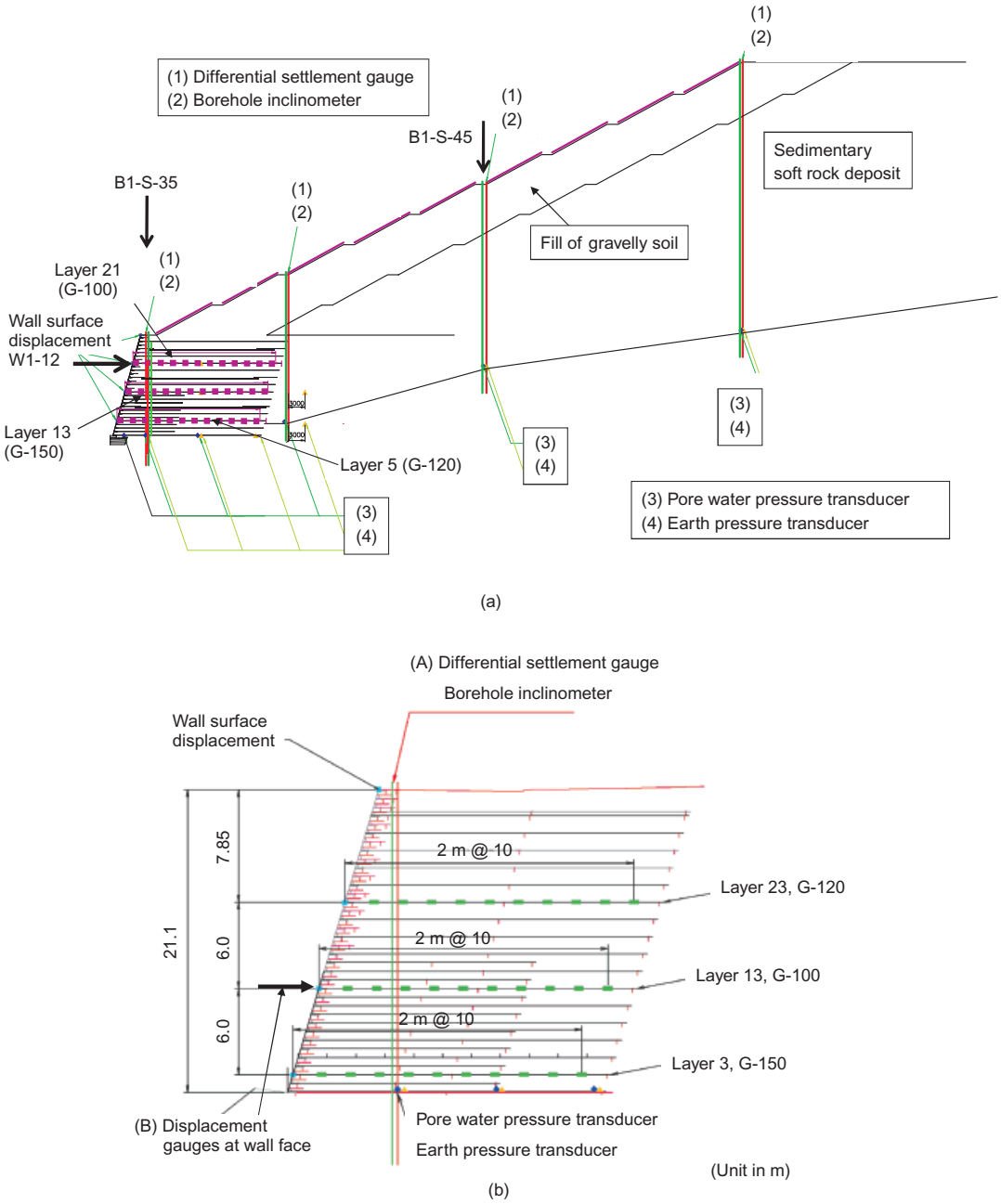

Figure 5. Typical cross-sections showing the locations of geogrid reinforcement layers equipped with electric-resistance strain gauges, displacement gauges and others: (a) 16.7 m high GRS wall in valley 1; and (b) 21.1 m high GRS wall in valley 2 (modified from Fujinami *et al.* 2007; Fujita *et al.* 2007; Takagi *et al.*, 2007)

Table 1. Strength properties of three representative geogrid types used to construct the walls

Geogrid type	Ultimate tensile strength (strain rate = 1 %/min) (kN/m)	Design tensile strength T_A (after applying creep reduction factor, 1.6)* (kN/m)	Layer no. (see Figures 5(a) and (b)	
			16.7 m high wall	21.1 m high wall
G-100	95	59	21	13
G-120	112	70	5	23
G-150	140	87	13	3

*Installation damage factor = 1.0; and durability reduction factor = 1.0.

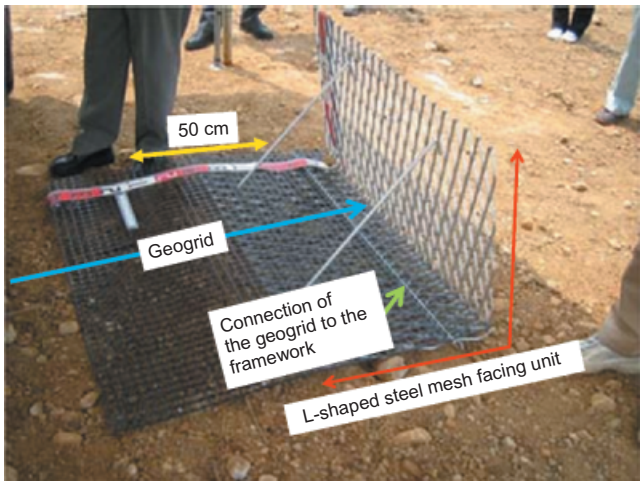

Figure 6. L-shaped facing unit of galvanized expanded metal mesh to protect the wall face

geogrid reinforcement layers were connected to the bottom part of the facing unit. The wall face was vegetated, as seen from Figure 1(d), by taking advantage of openings in the front part of the L-shaped facing unit.

Figures 5(a) and (b) show the instrumentation to monitor the wall performance during and after wall construction, including electric-resistance strain gauges installed on three selected geogrid layers in the respective walls, geogrid layers Nos. 5, 13 and 21 in the 16.7 m high GRS wall in valley 1 and Nos. 3, 13 and 23 in the 21.1 m high GRS wall in valley 2 (Figures 7(a) and (b)). Ten to thirteen electric-resistance strain gauges were arranged in the respective geogrid layers to obtain length-wise distributions. The geogrid tensile strains were evaluated from outputs of the electric-resistance strain gauges based on the calibration made by in-air tensile loading tests in the laboratory, in which the relationships between the outputs of the electric-resistance strain gauges and the average tensile strains from tensile deformation for a gauge length equal to 5 cm were obtained (see Figure 4(a)).

The observed performance of the two GRS walls is presented in Figures 8 and 9. It may be seen that the deformation of the walls during construction was very small (see Figure 5 for the locations of measurements). The total vertical compression of the backfill during construction was only 0.3% (the wall in valley 1) and 0.5% (the wall in valley 2) of the respective completed wall heights. Furthermore, the post-construction residual deformation of the two walls was negligible. In particular, the deformation due to a number of heavy rainfall events that took place after the end of wall construction was negligible. This very good performance was due largely to the fact that the reinforced backfill was compacted very well (Figure 3(b)). It should be noted that the compaction efficiency is generally higher when the backfill is reinforced than when it is not, because lateral yielding of the backfill when subjected to heavy compaction load is better restrained when reinforcement is present. It is very likely that effective drainage systems arranged inside and at the base of the backfill worked very well. These results, showing a very high stability of the two walls under static

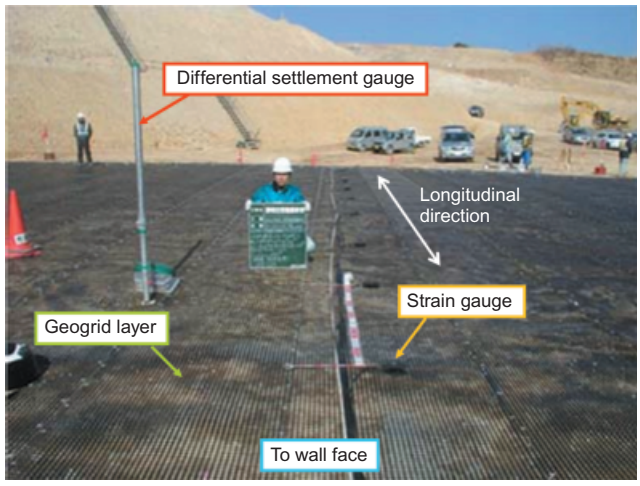

(a)

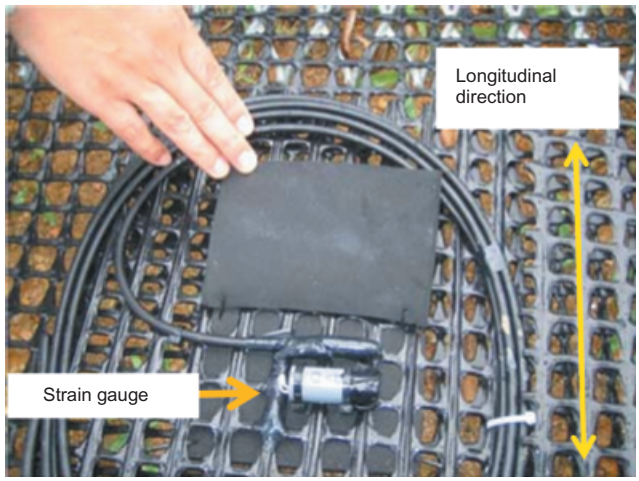

(b)

Figure 7. Installation of electric-resistance strain gauges in the 21.1 m high GRS wall in valley 2: the connection cables for data acquisition are extended toward the wall face: (a) general view (modified from Fujinami *et al.* 2007); and (b) a close-up

loading conditions even during heavy rainfalls, indicate that long-term residual deformation of soil structures can be restrained effectively by good compaction of high-quality backfill and arrangement of effective drainage systems even when reinforced with so-called extensible reinforcement, such as a polymeric geogrid. On the other hand, relatively large compression took place during and after construction of the embankment constructed on the slope in valley 1 (Figure 5(a)). This was probably due to the fact that the backfill was not reinforced, the compaction work was on a slope, which was relatively difficult, and a larger compacted lift (equal to 40 cm) was employed, despite the use of heavier compaction machines (18 tonf-class vibratory compactors).

3. TENSILE LOADING TESTS OF GEOGRIDS

In each of the walls, electric-resistance strain gauges were attached to three typical geogrid layers using three types of geogrid, G-100, G-120 and G-150. Table 1 summarises

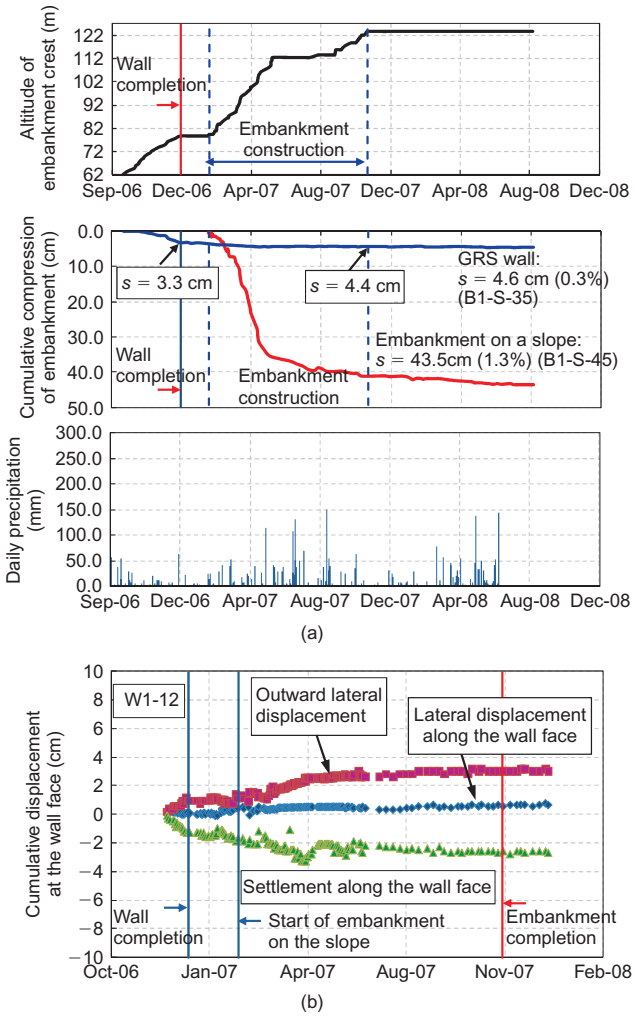

Figure 8. (a) Settlement at the crest of wall (location B1-S-35 in Figure 5(a) and mid-point of the embankment on the slope (location B1-S-45) in valley 1; and (b) displacements at the wall face (location W1-12 in Figure 5(a) during and after construction of the wall in valley 1 (modified from Fujinami *et al.* 2009; Fujita *et al.* 2007, 2008; Takagi *et al.* 2007)

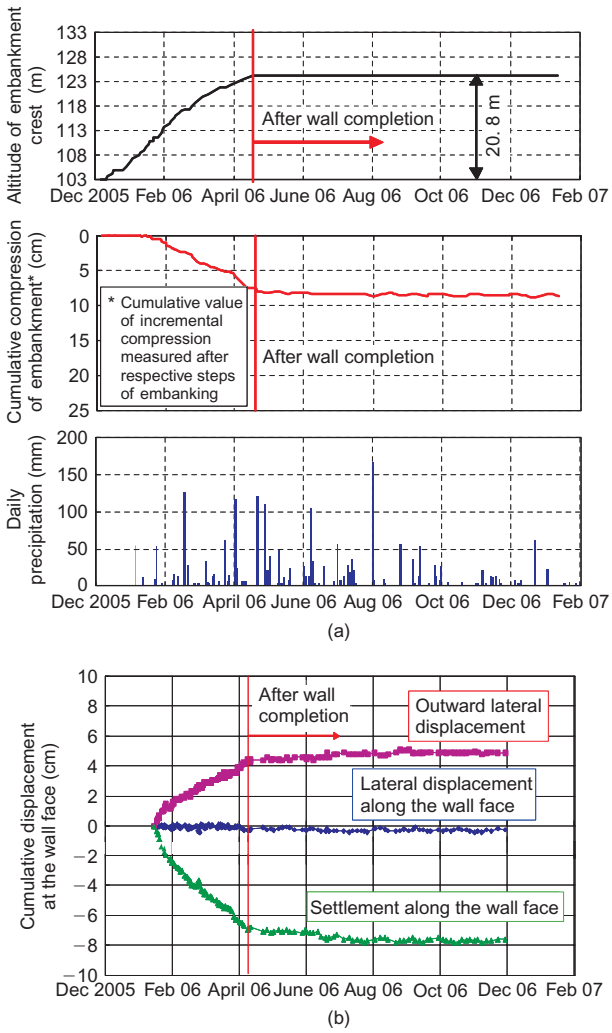

Figure 9. (a) Settlement at the crest of wall (location A in Figure 5(b)); and (b) displacements at the wall face (location B in Figure 5(b)) during and after construction of the wall in valley 2 (modified from Fujinami *et al.* 2007; Fujita *et al.* 2007, 2008; Takagi *et al.* 2007)

their ultimate tensile strengths obtained by fast tensile loading tests at a strain rate of 1.0%/min using 22.4 cm wide specimens of new product. The design rupture strengths were obtained by reducing these fast loading tensile strengths of new product using a creep reduction factor equal to 1/0.625 = 1.6 (determined on the basis of a number of creep loading tests, reported by the manufacturer). The tensile loading tests were also performed on geogrid specimens that were retrieved from trial fills where the backfill in which the geogrid layers had been installed was compacted in the same way as the actual construction work of the two walls. The installation damage factor was confirmed to be essentially equal to unity based on these tensile loading test results. The durability reduction factor to account for long-term degradation by negative chemical or biological effects was taken to be equal to unity, based on results from the degradation tests performed by the manufacturer and field conditions at the site, where no serious negative chemical or biological effects are likely.

Figures 10(a) and (b) show the tensile load–tensile strain (T–ε) relations and time histories of tensile strain from unconventional load-controlled tensile loading tests on new products performed by using the apparatus shown in Figure 4 and the test methods reported by Hirakawa *et al.* (2003) and Kongkitkul *et al.* (2004, 2007a). That is, sustained loading were performed for 12 h at two tensile load levels (T) equal to 6.5 and 13 kN/m during otherwise monotonic loading (ML) at a load rate of 0.0018 kN/m per min. Creep deformation is noticeable even at these low tensile load levels, which are considerably below the respective ultimate tensile strengths (Table 1). The simulations presented in these figures are explained later.

4. GEOGRID TENSILE STRAINS MEASURED IN THE WALLS

Figures 11(a), (b) and (c) show time histories of the tensile strain measured in geogrid layer Nos. 5 (G-120), 13 (G-150) and 21 (G-100) in the 16.7 m high GRS wall in

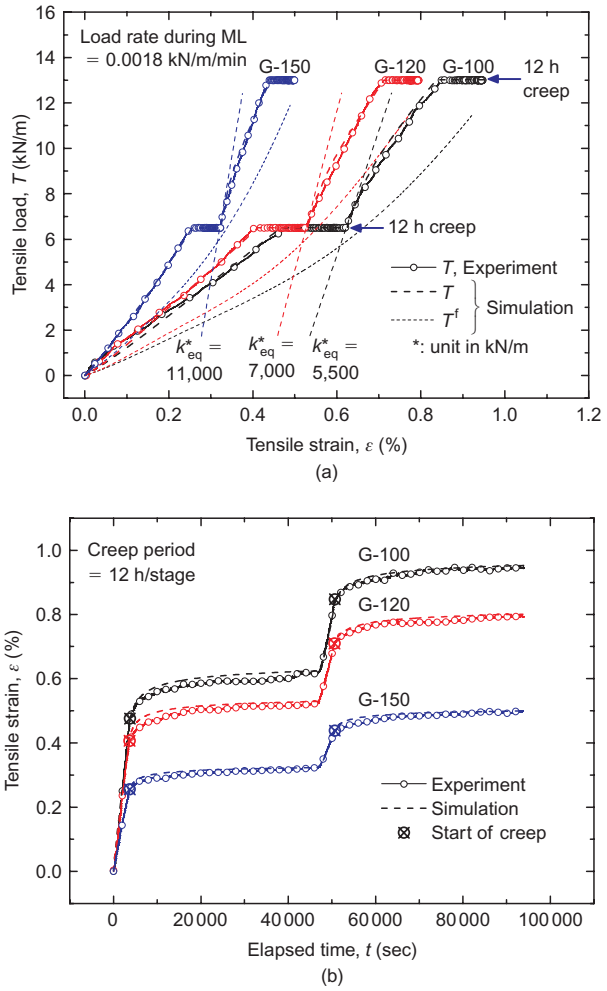

Figure 10. In-air tensile test results and model simulations: (a) tensile load-strain relations; and (b) time histories of tensile strain

valley 1. Figures 12(a), (b) and (c) show similar measurements in geogrid layers Nos. 3 (G-150), 13 (G-100) and 23 (G-120) in the 21.1 m high GRS wall in valley 2. The origin of elapsed time was defined when the respective geogrid layers were installed. Figures 13 and 14 show the distributions of geogrid strains at selected moments, corresponding to Figures 11 and 12. It should be noted that the locally measured tensile strain values presented in Figures 11 and 12 are time-dependent due not only to the viscous property of the geogrid but also the backfill as well as interactions between them. The following trends of behaviour may be seen from these figures.

1. The rate of increase of tensile strain was high during wall construction. The increase at a high rate stopped when the wall was completed in most of the monitored geogrid layers.
2. The tensile strain mobilised at the end of wall construction in the respective geogrid layers was largest at 2 m back from the wall face in all the geogrid layers, except for geogrid layer No. 3 (the lowest layer) in valley 2 (Figure 14(a)), where the strain was largest at 10 m back from the wall face. In geogrid layer Nos. 13 and 23 in the wall in valley 2 (Figures 14(b) and (c)), the strains at 4 and 8 m, respectively, from the wall face were also largest although they were similar to those at 2 m from the wall face in the respective layers. This observation indicates that there was no deep global potential failure plane as a sign of global unstable behaviour of these two walls. Considering that the distributions of strain in the respective geogrid layers were rather irregular, to capture the general trend of the time-dependency of strain and force in the geogrid layers, the average of all the measured values in the respective geogrid layers was obtained, as shown in Figures 11 and 12.
3. After the end of wall construction, the geogrid strains continued increasing at some locations, but the rate of increase was very low. At the other locations, the geogrid strain stopped increasing and at some locations, the geogrid tensile strain even started to decrease with time. These trends of behaviour were consistent with those observed in the PSC tests on geosynthetic-reinforced sand specimens reported by Kongkitkul *et al.* (2008a). The general trend of behaviour of the tensile strain in the geogrid after the end of wall construction was consistent with very small or negligible residual deformation of the walls after the end of construction, as seen from Figures 8 and 9.
4. The observed geogrid strains were substantially lower than the strain at rupture. Therefore, the tensile forces obtained by substituting these strains into the measured load–strain relations shown in Figure 10(a) were substantially lower than the respective tensile rupture strengths listed in Table 1.

5. MODELLING OF RATE-DEPENDENT LOAD–STRAIN BEHAVIOUR OF GEOGRID

Di Benedetto *et al.* (2002), Tatsuoka *et al.* (2002, 2008) and Kongkitkul *et al.* (2008c) proposed a non-linear three-component model to simulate the elasto-viscoplastic stress–strain behaviour of geomaterial. Hirakawa *et al.* (2003) and Kongkitkul *et al.* (2004, 2007a) modified the model to simulate the rate-dependent tensile load–tensile strain behaviour of polymeric geosynthetic reinforcement (Figure 15) and showed that the model can simulate very accurately the rate-dependent load–strain behaviours, including stress jumps by stepwise changes in the strain rate, creep strain during sustained loading and stress relaxation, of many different types of polymeric reinforcement, as typically shown in Figure 4(d). Kongkitkul and Tatsuoka (2007) and Kongkitkul *et al.* (2007d), respectively, modified the model to take into account the effects of ambient temperature and time-dependent degradation on the load–strain behaviour of polymeric geosynthetic reinforcement.

According to the model (Figure 15), the tensile load T at a given irreversible strain, ε^{ir}, ($[T]_{(\varepsilon^{ir})}$) is obtained by adding the viscous component ($[T^{v}(\varepsilon^{ir}, \dot{\varepsilon}^{ir}, h_s)]_{(\varepsilon^{ir})}$) to the inviscid component ($[T^{f}(\varepsilon^{ir})]_{(\varepsilon^{ir})}$) at the same ε^{ir}, while

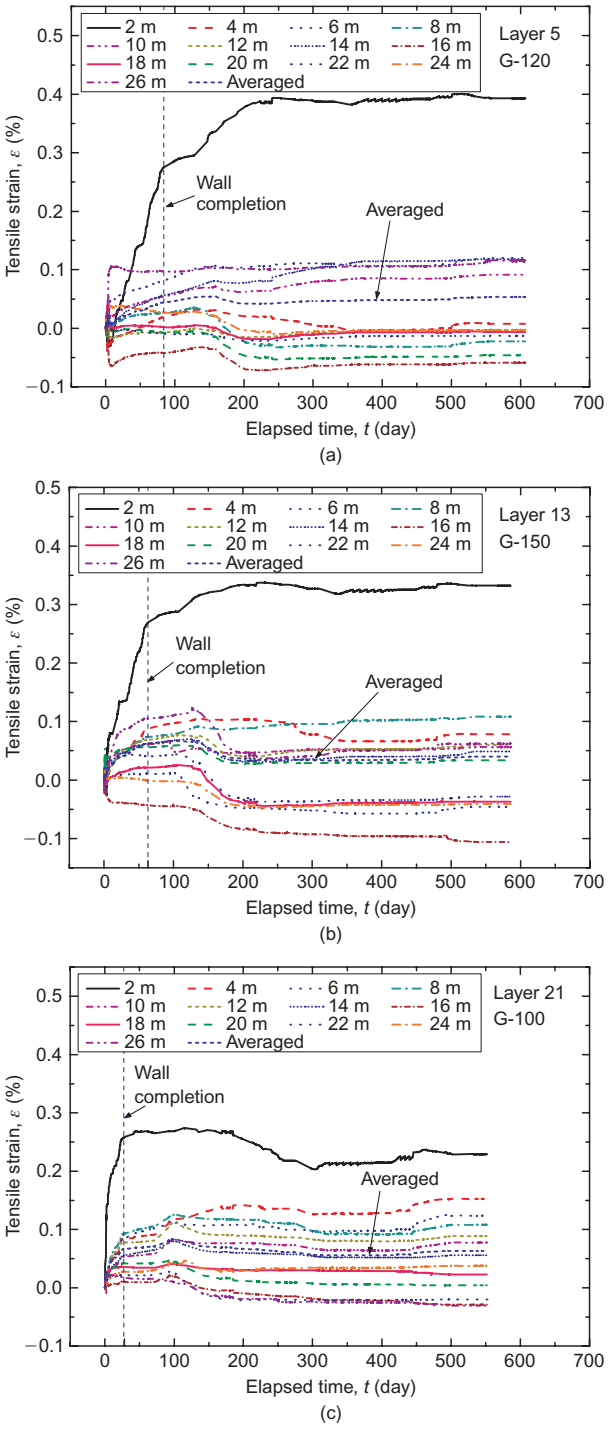

Figure 11. Time histories of individual and average tensile strains in the three geogrid layers in the 16.7 m GRS wall in valley 1: layer Nos. (a) 5 (G-120); (b) 13 (G-150); and (c) 21 (G-100); the distances (in m) are back from wall face

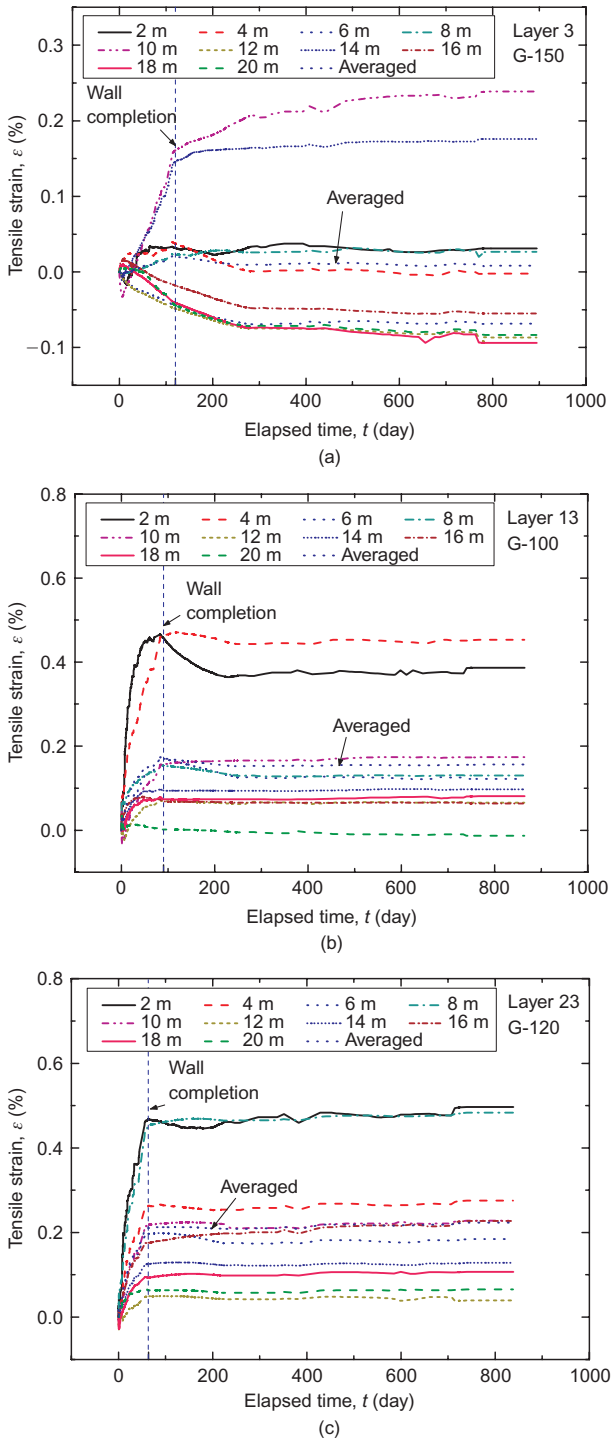

Figure 12. Time histories of individual and average tensile strains of geogrid layers in the 21.1 m GRS wall in valley 2: layer Nos. (a) 3 (G-150); (b) 13 (G-100); and (c) 23 (G-120); the distances (in m) are back from wall face

the tensile strain rate ($\dot{\varepsilon}$) by adding the elastic component $\dot{\varepsilon}^{\mathrm{e}}$ to the irreversible component $\dot{\varepsilon}^{\mathrm{ir}}$ at the same T, as:

$$[T]_{(\varepsilon^{\mathrm{ir}})} = [T^{\mathrm{f}}(\varepsilon^{\mathrm{ir}})]_{(\varepsilon^{\mathrm{ir}})} + [T^{\mathrm{v}}(\varepsilon^{\mathrm{ir}}, \dot{\varepsilon}^{\mathrm{ir}}, h_{\mathrm{s}})]_{(\varepsilon^{\mathrm{ir}})} \quad (1a)$$

$$\dot{\varepsilon} = \dot{\varepsilon}^{\mathrm{e}} + \dot{\varepsilon}^{\mathrm{ir}} \quad (1b)$$

where h_{s} is the loading history parameter, which is not necessary for the Isotach viscous property under ML conditions. Kongkitkul *et al.* (2008b) reported that the geogrid made of Aramid fibre, used for the two walls, exhibits the Isotach viscous property. In that case, $[T^{\mathrm{v}}(\varepsilon^{\mathrm{ir}}, \dot{\varepsilon}^{\mathrm{ir}})]_{(\varepsilon^{\mathrm{ir}})}$ is obtained as:

$$[T^{\mathrm{v}}(\varepsilon^{\mathrm{ir}}, \dot{\varepsilon}^{\mathrm{ir}})]_{(\varepsilon^{\mathrm{ir}})} = [T^{\mathrm{f}}(\varepsilon^{\mathrm{ir}})]_{(\varepsilon^{\mathrm{ir}})} \cdot g_{\mathrm{v}}(\dot{\varepsilon}^{\mathrm{ir}}) \quad (2a)$$

$$g_{\mathrm{v}}(\dot{\varepsilon}^{\mathrm{ir}}) = \alpha^{*} \cdot \left(|\dot{\varepsilon}^{\mathrm{ir}}|/\dot{\varepsilon}_{0}^{\mathrm{ir}}\right)^{1+b^{*}} \quad (2b)$$

where $g_{\mathrm{v}}(\dot{\varepsilon}^{\mathrm{ir}})$ is the viscosity function, which is a highly non-linear function of the irreversible strain rate $\dot{\varepsilon}^{\mathrm{ir}}$; and

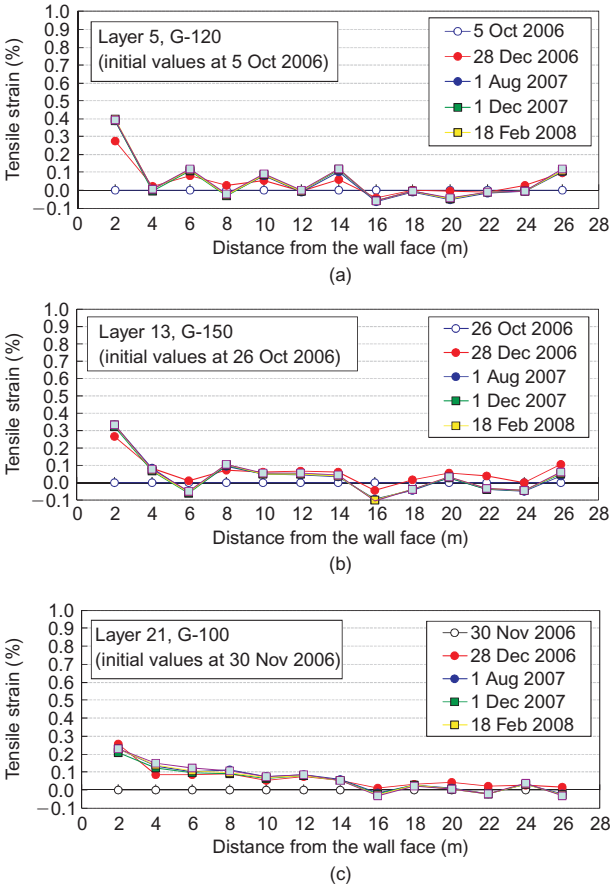

Figure 13. Distributions of tensile strain in the three geogrid layers in the 16.7 m GRS wall in valley 1: layer Nos. (a) 5 (G-120); (b) 13 (G-150); and (c) 21 (G-100)

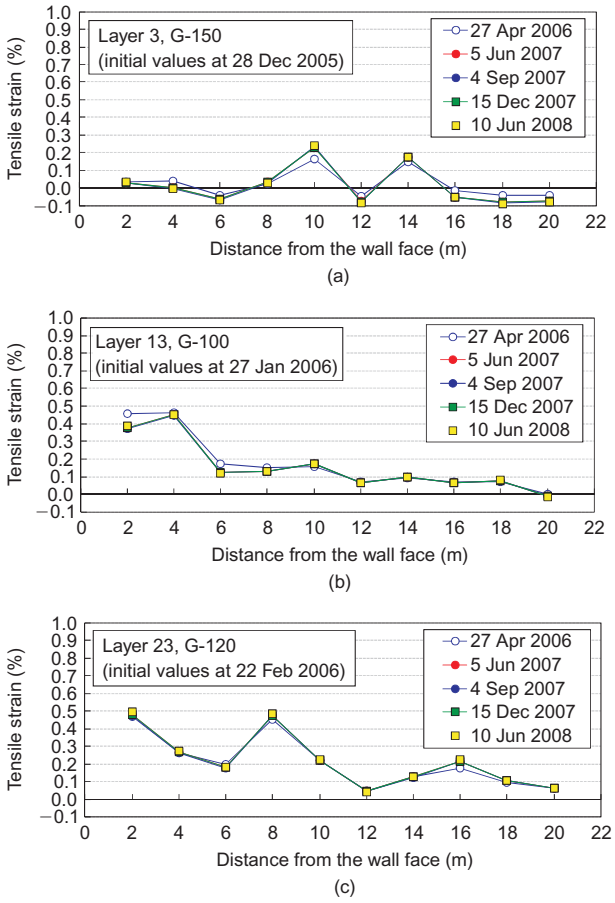

Figure 14. Distributions of tensile strain of geogrid layers in the 21.1 m GRS wall in valley 2: layer Nos. (a) 3 (G-150); (b) 13 (G-100); and (c) 23 (G-120)

α^*, b^* and $\dot{\varepsilon}_0^{\mathrm{ir}}$ are the material constants. Kongkitkul *et al.* (2007a, 2008a) showed that Equation 2b, which was originally proposed by Di Benedetto *et al.* (1999, 2005) to simulate creep deformation of sand, is also relevant to simulate the creep behaviour of geosynthetic reinforcement after the strain rate becomes very low (see Appendix A for the details). By analysing the test results of this geogrid type consisting of Aramid fibre by Hirakawa *et al.* (2003), partly shown in Figure 4(c), the parameters $\alpha^* = 0.18$, $b^* = -0.65$ and $\dot{\varepsilon}_0^{\mathrm{ir}} = 10^{-6}$ %/s were obtained. It was found that these parameters were also relevant to the three types of Aramid geogrid along which tensile strains were measured in the two walls. The elastic properties of the three types of geogrid were determined from the respective T–ε relations immediately after the restart of ML at the end of sustained loading, as shown in Figure 10(a). The T^{f}–ε relations (i.e. the reference relations) of the three types of geogrid, which are the T–ε relations when $\dot{\varepsilon}^{\mathrm{ir}} = 0$, were determined as shown in Figure 10(a). It may be seen that not only the load–strain relations (Figure 10(a)) but also the time histories of creep strain (Figure 10(b)) were simulated very well by the model using these model parameters.

6. ESTIMATION OF GEOGRID TENSILE FORCES

To obtain the time histories of tensile force of the six geogrid layers by the non-linear three-component model

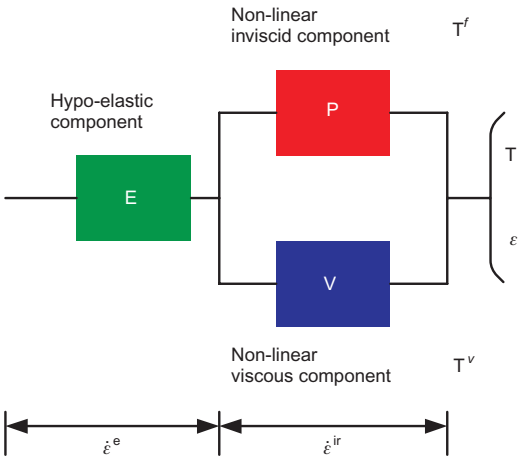

Figure 15. Non-linear three-component model modified for polymeric geosynthetic reinforcement (after Hirakawa *et al.* 2003; Kongkitkul *et al.* 2004, 2007a)

(Figure 15), the time histories of respective measured tensile strains as well as their average in the respective monitored geogrid layers were fitted by empirical equations. Figures 16(a) and (b) show the time histories of tensile strain defined as zero at the end of wall construction at 2 m back from the wall face in geogrid layer No. 13 (G-150) of the wall in valley 1 and at 10 m back from the wall face in geogrid layer No. 3 (G-150) of the wall in

valley 2, respectively. These time histories are typical of those that exhibited a continuous increase with time (Figures 11 and 12). To alleviate difficulties in the subsequent analysis of the data due to irregular variations with time in the respective time histories of strain, Equation 3(a) was fitted to the data to obtain smooth time histories, as shown in Figures 16(a) and (b):

$$\Delta\varepsilon = A_1 \cdot \left(1 - \mathrm{e}^{-\Delta t/t_1}\right) + A_2 \cdot \left(1 - \mathrm{e}^{-\Delta t/t_2}\right) \tag{3a}$$

$$\dot{\varepsilon} = \frac{\partial \varepsilon}{\partial t} = \frac{A_1 \cdot \mathrm{e}^{-\Delta t/t_1}}{t_1} + \frac{A_2 \cdot \mathrm{e}^{-\Delta t/t_2}}{t_2} \tag{3b}$$

where A_1, A_2, t_1 and t_2 are constants. Equation 3(b) was obtained by differentiating Equation 3(a) with respect to time.

Figure 17(a) (in the full-log plot) shows the time histories of tensile strain rate at the selected locations of the three geogrid layers of the wall in valley 1 represented by Equation 3(b) that was obtained from Equation 3(a) fitted to the data. Figure 17(b) shows the averaged relations of the respective layers. Figures 18(a) and (b) show similar results of the wall in valley 2. It is to be noted that the averaged value in geogrid layer No. 13 of the wall in valley 1, the local value at 4 m back from the wall face in geogrid layer No. 13 and the averaged values in geogrid layer Nos. 3 and 13 of the wall in valley 2 exhibit negative strain rates, which means that the respective geogrid strains decreased with time after the end of wall construction. In all these cases, the absolute value of geogrid strain rate decreased at a high rate with time. The respective time histories of tensile strain rate represented by Equation 3b and shown in Figures 17 and 18 were extrapolated towards the end of the design life typical for civil engineering structures (i.e. 50 years) in the analysis shown below.

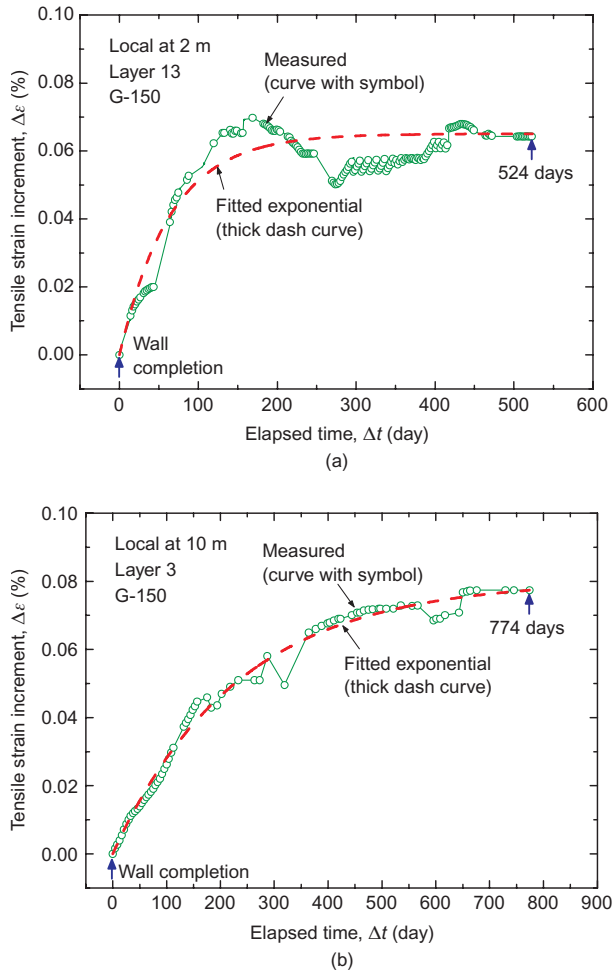

Figure 16. Measured and fitted time histories of tensile strain increment of G-150 geogrid at: (a) 2 m back from the wall face in layer No. 13 of the 16.7 m high GRS wall in valley 1; and (b) 10 m back from the wall face in layer No. 3 of the 21.1 m high GRS wall in valley 2.

The time histories of tensile force of the monitored geogrids in the two walls were estimated by the non-linear three-component model from the fitted time histories of tensile strain rate until the end of observation (i.e., 524 and 774 days, respectively, for the walls in valley 1 and valley 2). The time histories were then extrapolated to 50 years based on the relations fitted by Equation 3. Therefore, the effects of the viscous properties of both geogrid and backfill as well as their interactions were involved in these extrapolated time histories. Figures 19(a), (b) and (c) show the relationships between the estimated tensile force and the measured local tensile strain (fitted by Equation 3a) before and after the end of wall construction at selected locations in the three monitored geogrid layers in the wall in valley 1 (see Figure 5(a) for their locations). Figures 20(a), (b) and (c) show similar relations for the averaged strains in these geogrid layers (Figure 17(b)). Similarly, Figures 21(a), (b) and (c) show the local relations at selected locations in the three monitored geogrid layers in the wall in valley 2 (see Figure 5(b) for their locations). Figures 22(a), (b) and (c) show the relations for the averaged strains in these geogrid layers in the wall in valley 2 (Figure 18(b)).

The solid curves presented in Figures 19 to 22 show the T–ε relations starting at the origin (0,0) (defined as when the respective geogrid layers were installed) and obtained from the measured time histories of tensile strain by extrapolation to 50 years. The dotted curves represent the relations if ML had continued even after the end of wall construction at the strain rate pertaining at the end of the construction phase. In all the solid curves, immediately after the end of wall construction, the loading condition (where $\dot{\varepsilon}^{\mathrm{ir}} > 0$) was maintained. Subsequently, in some cases, the loading condition continued to the end of 50 years. In some other cases, the neutral state (where $\dot{\varepsilon}^{\mathrm{ir}} = 0$), which is located on the reference relation for loading, was then reached. In some cases, the sign of irreversible strain rate, $\dot{\varepsilon}^{\mathrm{ir}}$, then changed to be negative and the tensile load–strain behaviour entered into an unloading branch (where $\dot{\varepsilon}^{\mathrm{ir}} < 0$). The analyses under the unloading conditions by the three-component model (Figure 15) were made on the basis of the respective reference relations for the unloading conditions, which were determined following the method explained in Appendix B (Kongkitkul *et al.* 2004, 2008a).

Figures 19(a) and (b) show the estimated T–ε relations in the two cases where the geogrid was locally most

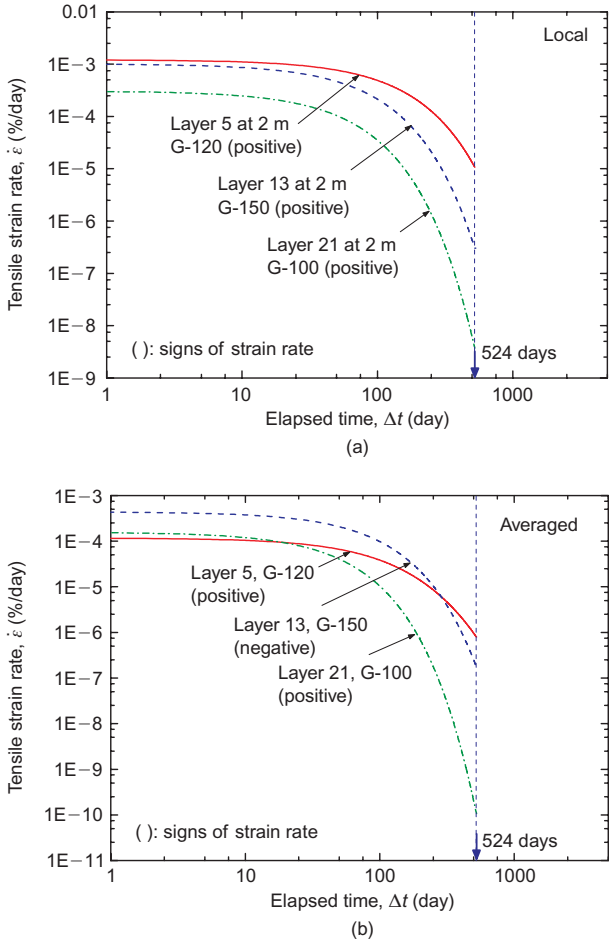

Figure 17. Geogrid strain rate–elapsed time relations from the fitted time histories of tensile strain of geogrids in the 16.7 m GRS wall in valley 1: (a) local at selected locations; and (b) average in the respective layers

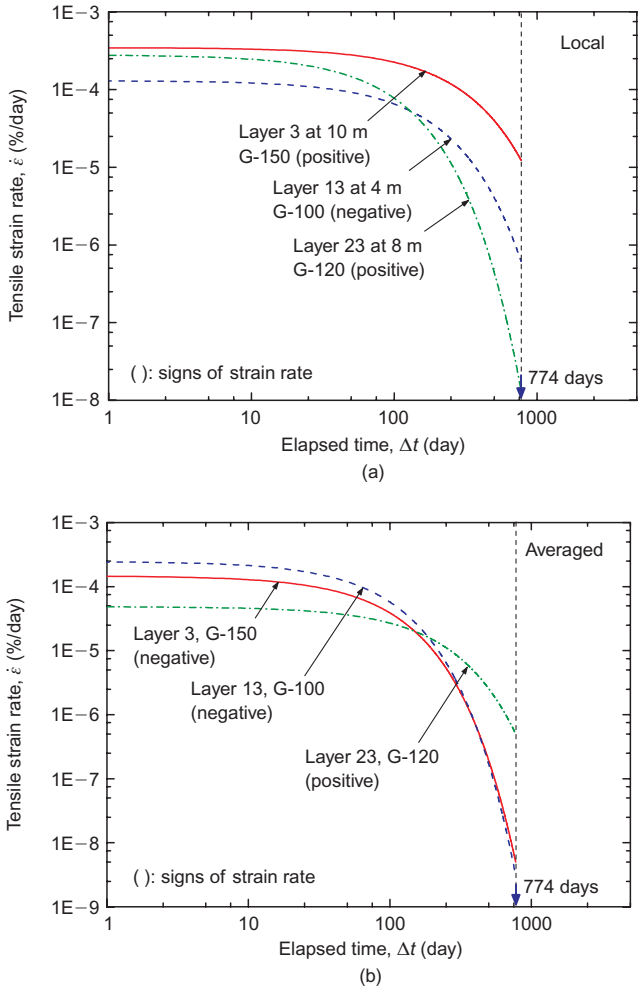

Figure 18. Geogrid strain rate–elapsed time relations from the fitted time histories of tensile strain of geogrids in the 21.1 m GRS wall in valley 2: (a) local at selected locations; and (b) average in the respective layers

severely loaded among those analysed in the wall in valley 1. Figure 21(a) shows a similar case in the wall in valley 2. In these cases, after the end of wall construction, the tensile strain continued increasing with time at such a relatively high rate that the geogrid tensile force also continuously increased with time. It should be noted that, in valley 1 (Figure 1(c)), a 45 m high sloped embankment was constructed behind the 16.7 m high GRS wall for a period of about 9 months starting about 2 months after the end of wall construction (Figure 8). It seems that the geogrid tensile strain was somehow increased by the load from the sloped embankment for some period after the end of wall construction, unlike the wall in valley 2. The predicted tensile forces after 50 years were, however, only about 4.32 and 6.49 kN/m, respectively, for geogrid layer Nos. 5 and 13 of the wall in valley 1 and about 4.25 kN/m for geogrid layer No. 3 in the wall in valley 2. These values are substantially lower than the respective design ultimate tensile strengths (Table 1). If the geogrid was damaged when installed in the backfill, then because the geogrid tensile forces were estimated using model parameters determined by laboratory tensile loading tests using new products, these estimated geogrid tensile forces would overestimate the true values. It was confirmed, however, that the installation damage was negligible, although the conclusion above would not change even if the installation damage cannot be ignored.

Figures 23, 24 and 25 show the time histories of the estimated tensile force based on the measured and fitted tensile strain representing the cases presented in Figures 19 to 22, which are typical of the geogrid behaviour in the two walls. The time histories of geogrid force when the strain was assumed to be kept constant after the end of wall construction (i.e. load relaxation behaviour), and those when the tensile force was assumed to be kept constant (i.e. creep behaviour), are also presented for reference. It can be seen that the actual behaviour was much more complicated than these two idealised cases.

In the relations plotted in Figures 19(c) and 20(c) (the wall in valley 1) and Figures 21(c) and 22(c) (the wall in valley 2), the tensile strain rate increased with time after the end of wall construction, as in the cases presented in Figures 19(a) and (b) and Figure 21(a). However, the estimated T–ε relations exhibited first a sudden immediate decrease in the tensile force, which was followed by a very slow increase in the tensile force with time. As a result, the total increase in the geogrid tensile force was much smaller. Even after 50 years, the estimated tensile

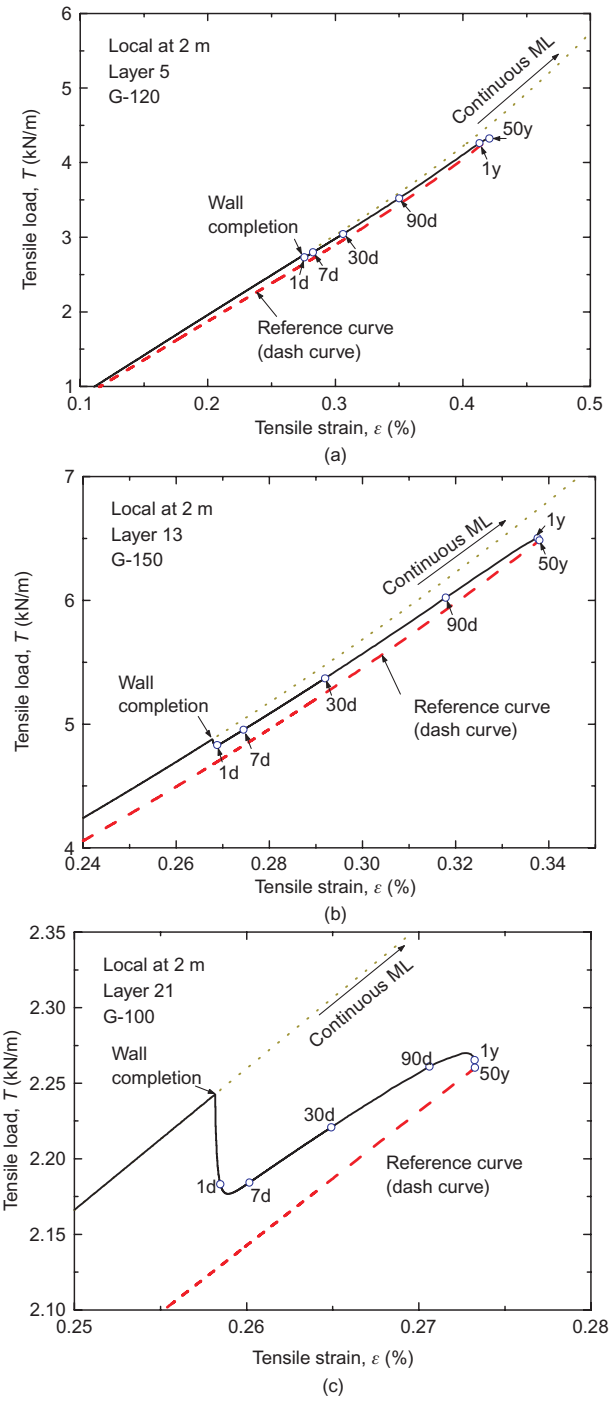

Figure 19. Tensile load–local tensile strain relations of geogrid at selected locations in the 16.7 m high GRS wall in valley 1, extrapolated to 50 years, in layer Nos.(a) 5 (G-120); (b) 13 (G-150); and (c) 21 (G-100)

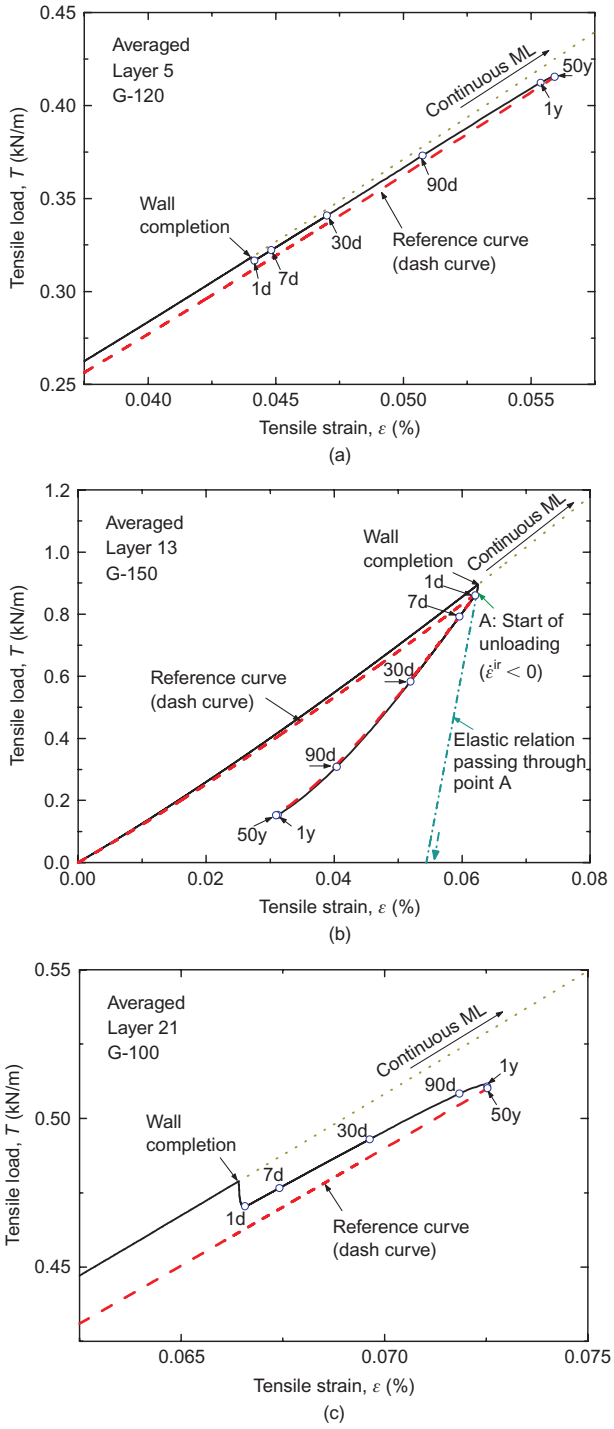

Figure 20. Tensile load–average tensile strain relations of geogrid arranged in the 16.7 m high GRS wall in valley 1, extrapolated to 50 years, in layer Nos. (a) 5 (G-120); (b) 13 (G-150); and (c) 21 (G-100)

force was only slightly higher than the value at the end of wall construction. This trend of post-construction behaviour in geogrid layer No. 21 of the wall in valley 1 and geogrid layer No. 23 in the wall in valley 2 was similar to the one observed in the PSC tests on small-size geogrid-reinforced sand specimens reported by Kongkitkul *et al.* (2007c). These trends of behaviour can also be clearly seen from Figures 23 and 24.

On the other hand, as seen from Figure 20(b) (the wall in valley 1) and Figure 21(b) and Figure 22(a) and (b) (the wall in valley 2), the geogrid tensile force significantly decreased with time due to consistently negative strain rates after the end of wall construction (Figures 17 and 18). In these cases, the tensile force decreased firstly under the loading condition (where $\dot{\varepsilon}^{ir} > 0$), then under the unloading condition (where $\dot{\varepsilon}^{ir} < 0$). As a result, it is estimated that the geogrid tensile force decreased greatly and it is predicted that this unloading will also continue during coming many years. This trend of behaviour is similar to that observed in the PSC tests on large-size geogrid-reinforced sand specimens reported by Kongkitkul *et al.*

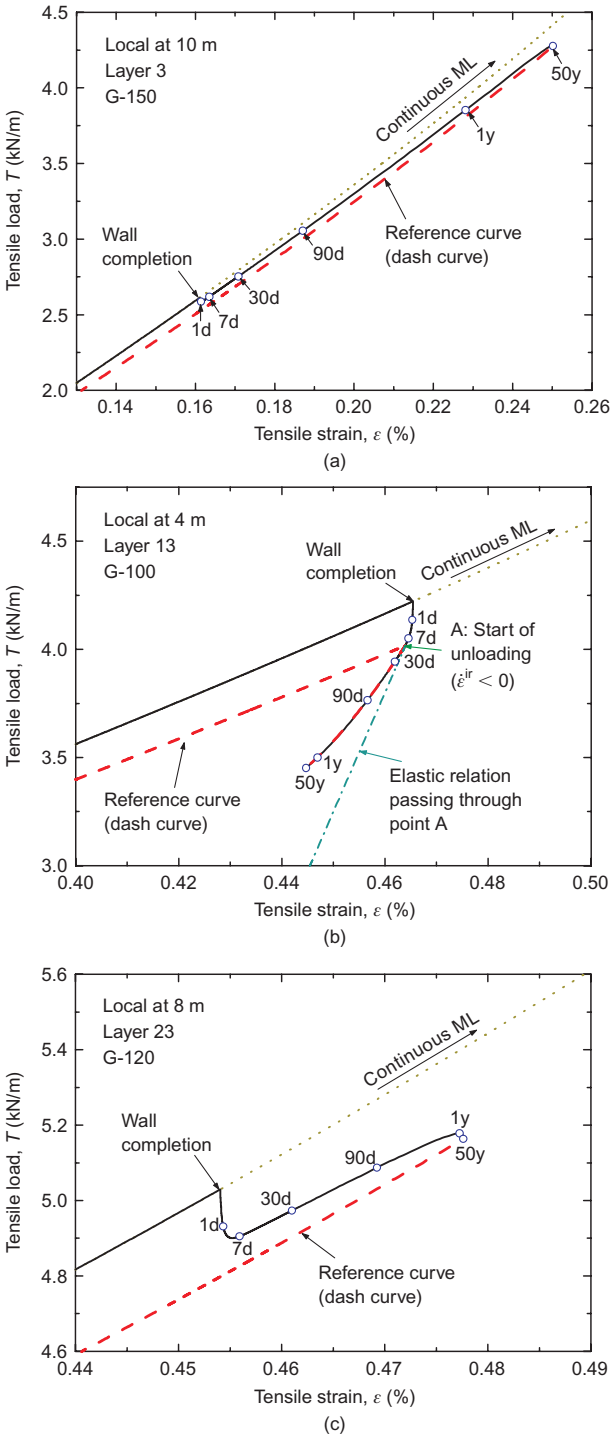

Figure 21. Tensile load–local strain relations of geogrid at selected locations in the 21.1 m high GRS wall in valley 2, extrapolated to 50 years, in layer Nos. (a) 3 (G-150); (b) 13 (G-100); and (c) 23 (G-120)

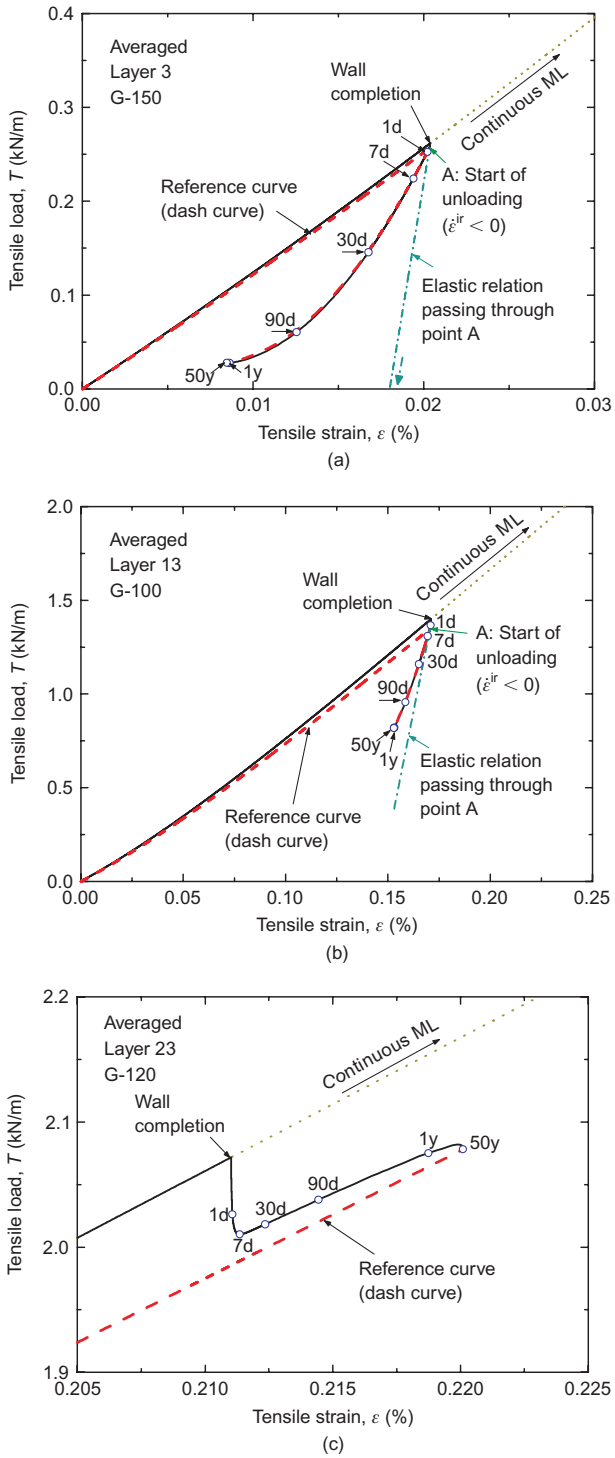

Figure 22. Tensile load–averaged strain relations of geogrid arranged in the 21.1 m high GRS wall in valley 2, extrapolated to 50 years, in layer Nos. (a) 3 (G-150); (b) 13 (G-100); and (c) 23 (G-120)

(2008a). In these cases, after the end of wall construction, the geogrid tensile force decreased at a rate that was much larger than the one that applied when the load-relaxation took place at a constant strain. Therefore, it is very likely that creep rupture failure was not likely to take place by the end of a lifetime equal to 50 years. The analysis presented above suggests that this estimate is also relevant when the lifetime is 100 years. As a final remark, as seen from these figures, when the purely elastic response under the unloading condition is assumed to take place, the decrease in the tensile force is largely over-estimated. These trends of behaviour can also be seen from Figure 25.

7. DISCUSSION

Summarising the above, it is very likely that, with the two high GRS walls, the geogrid tensile force would be kept to values that were substantially lower than the respective

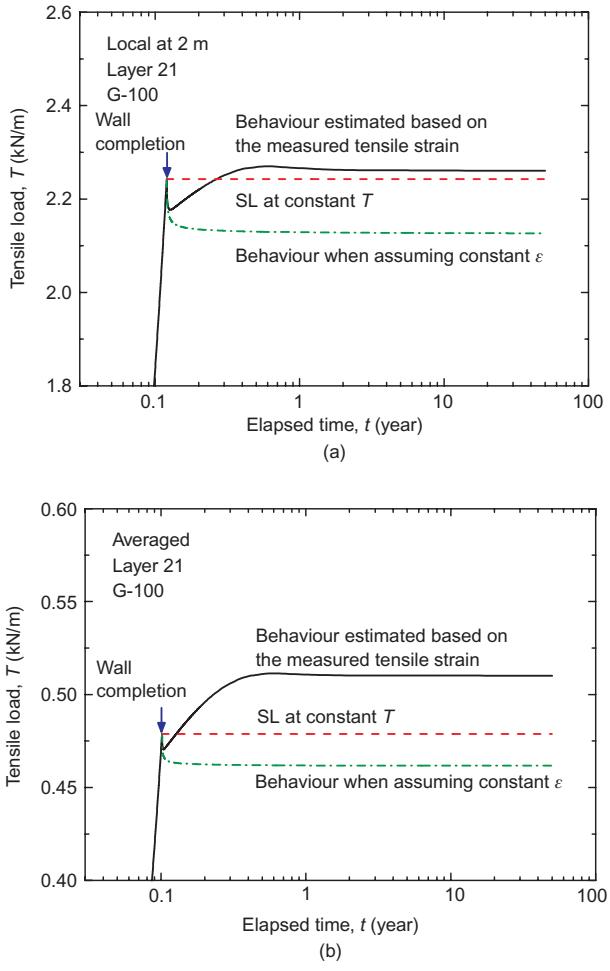

Figure 23. Estimated time histories of tensile force of geogrid layer No. 21 (G-100) and the behaviours at constant T and ε of the 16.7 m high GRS wall, based on: (a) the measured strain at 2 m back from wall face; and (b) the averaged strain

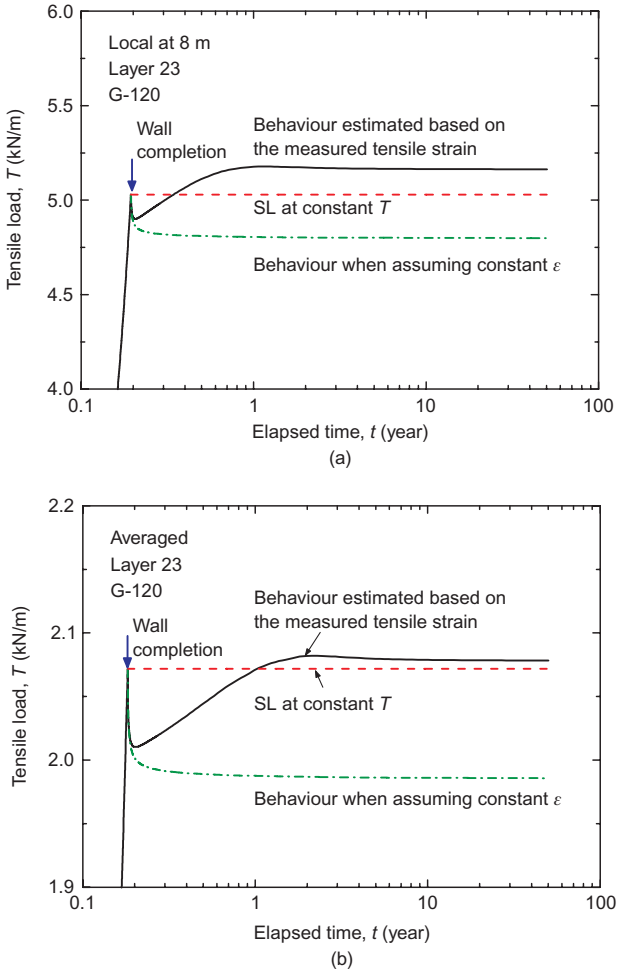

Figure 24. Estimated time histories of tensile force of geogrid layer No. 23 (G-120) and the behaviours at constant T and ε of the 21.1 m high GRS wall, based on: (a) the measured strain at 8 m back from wall face; and (b) the averaged strain

design ultimate tensile strengths by the end of a typical design life, 50 years. This behaviour is consistent with reports of a number of full-scale geosynthetic wall case histories by Allen and Bathurst (2002a, b). It should be noted that the method used to predict the mobilised tensile load in this study is different from the one used in their studies. In this study, an elasto-viscoplastic model that can predict the tensile load–strain relation from the measured tensile strain for any arbitrary loading history was used. On the other hand, in their studies, the mobilised tensile load was obtained by multiplying tensile strains using a suitably selected time-dependent reinforcement stiffness obtained from constant load creep tests (Bathurst *et al.* 2002; Walters *et al.* 2002). Their approach is applicable only for monotonically increasing or constant reinforcement load in the wall.

The relevance of the reinforcement force estimated for a long period after the end of strain observation presented herein depends on the reliability of both the extrapolated strains and the three-component model. It should be admitted that we need further research to fully validate the above. Even so, we consider that we can learn several important lessons. A very low increasing rate of estimated geogrid tensile force, or essentially zero increase or even a decrease in the estimated tensile force after the end of wall construction, as described above, is due first to a high safety factor against tensile rupture of the geogrid (as discussed later in this section). It is also due to the fact that not only the load–strain behaviour of polymeric geogrid reinforcement but also the stress–strain behaviour of backfill are rate-dependent due to their viscous properties. The reduction of tensile strain with time in the geogrid is due to compressive creep strains that take place in the horizontal direction in the backfill caused by the tensile force in the reinforcement (Tatsuoka *et al.* 2004). The observations and analyses presented in the preceding sections, as well as the considerations above, indicate that the possibility of excessive tensile deformation and eventual tensile creep rupture of the geogrid arranged in these two walls by the end of the prescribed design life is extremely low.

The above-mentioned trend of behaviour can also be expected with many other geosynthetic-reinforced soil retaining walls constructed using well-controlled backfill following similar construction procedures to those described in this paper. Bussert and Naciri (2009), among many others, also reported a number of case histories in which tensile strains activated in the HDPE geogrid

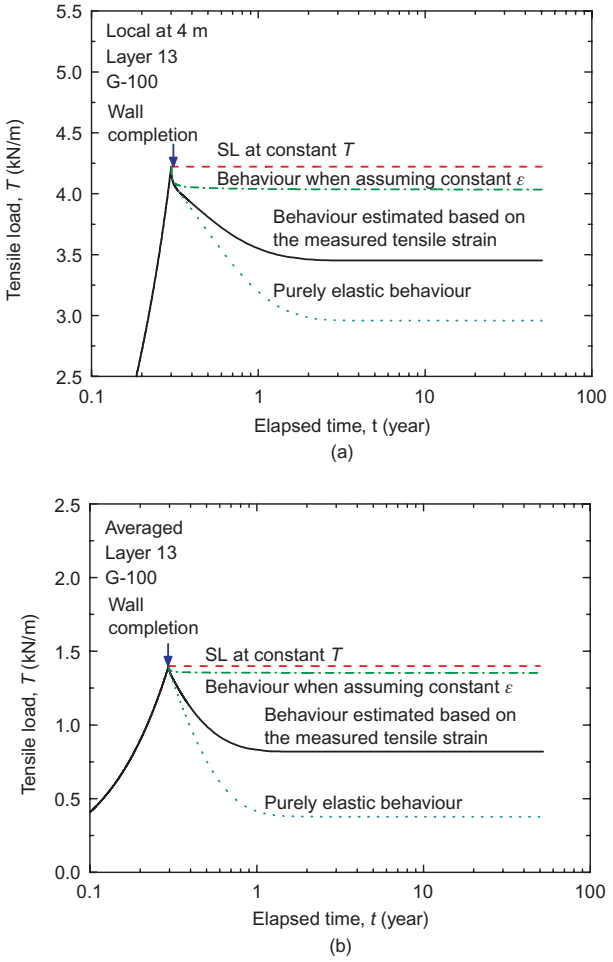

Figure 25. Estimated time histories of tensile force of geogrid layer No. 13 (G-100) and the behaviours at constant T and ε of the 21.1 m high GRS wall, based on: (a) the measured strain at 4 m back from wall face; and (b) the averaged strain

reinforcement placed in full-scale GRS retaining walls increased only at a very low rate, or were kept essentially constant, or even noticeably decreased, with time after the end of wall construction. However, in these case histories, no attempt was made to estimate the time histories of the geogrid force from measured time histories of the geogrid strain. The methodology to estimate the time histories of geogrid force described in this paper can be applied to other cases such as those referred to above.

The tensile forces that had been activated in the geogrid and those that would be activated under static loading conditions by the end of 50 years in the two walls were much lower than those predicted at the design stage. This means that the tensile forces that will be activated in the geogrid when the walls are subjected to design seismic loads would also be much lower than those predicted at the design stage. These considerations indicate that the design of the two walls was much more conservative than the one identified at the design stage. When an attempt was made to reduce the conservatism in the current design method (as usually used in practice and used for the design of the two walls) to a more relevant level and further to decrease the required rupture strength of the new polymeric geosynthetic reinforcement product for use for a given geosynthetic-reinforced soil retaining wall, two basic methods were identified. The first is to use a more realistic (i.e., higher) design shear strength value for the backfill. Then, using the same stability analysis method (usually the limit equilibrium-based stability analysis), the design working load of the geogrid is reduced. In the design of these two walls, an angle of internal friction equal to 35° and a cohesion intercept equal to 8.5 kPa, both under effective stress conditions, were used for the backfill. These design shear strength parameters of the backfill were obtained by conservative fitting of a linear failure envelope to multiple Mohr's circles of stress at failure from consolidated drained (CD) triaxial compression (TC) tests on saturated specimens of the backfill performed by a consulting firm. The specimens were obtained by compaction to a degree of compaction D_c for the modified Proctor equal to 90%, which was the allowable lower bound adopted in the field compaction control of the backfill during the construction of these two walls. These design shear strength parameters ($\phi = 35°$ and $c = 8.5$ kPa) are equivalent to a peak friction angle to the origin, $\phi_o = \arcsin[(\sigma'_1 - \sigma'_3)/(\sigma'_1 + \sigma'_3)]_{max}$, equal to 39° with $c = 0$ when $\sigma'_3 = 50$ kPa. On the other hand, Figure 26 summarises the relationships between ϕ_o and the degree of compaction D_c for the modified Proctor obtained from many series of CD TC and plane strain compression (PSC) tests performed at typical operated confining pressures in the field (mostly $\sigma'_3 = 50$ kPa). The specimens were made by using a wide variety of sandy and gravelly backfill actually used in construction projects. These TC and PSC tests were performed at the Tokyo University of Science (Hirakawa *et al.* 2008; Kiyota *et al.* 2009). The data from a new series of drained TC tests at $\sigma'_3 = 50$ kPa on specimens produced by compacting the gravelly soil ($D_{50} = 8.1$ mm; $U_c = 25.6$; and FC = 4.2 %) obtained by removing particles larger than 50.8 mm from the one used to construct these walls (Figure 2) at the optimum water content (for the modified Proctor) are included in these data. These TC tests were performed mainly after the construction of the two walls, independently of those performed at the design stage. The specimens during CD TC tests were either at the moist condition as compacted (i.e., the data points denoted by symbol ×) or after having been made fully saturated (i.e., the data points denoted by symbol +). It may be seen that the moist specimens are noticeably stronger than the saturated ones and this is probably due to the effects of suction. This fact indicates that the walls are more stable when not fully saturated. However, in the current design practice of soil structures in Japan, apparent cohesion due to suction of sandy and gravelly soils is ignored assuming fully saturated conditions, which was also the case with these two walls. It may also be seen that the design shear strength ($\phi_o = 39°$ with $c = 0$ when $\sigma'_3 = 50$ kPa) of the fully saturated specimens corresponds approximately to $D_c = 85\%$, which is even lower than the allowable lower bound (90%) in the field compaction control. On the other hand, as seen from Figure 3(b), the average values of the actual D_c values were 98 and 97.5% in the two walls, which were substantially higher than 85%. This fact

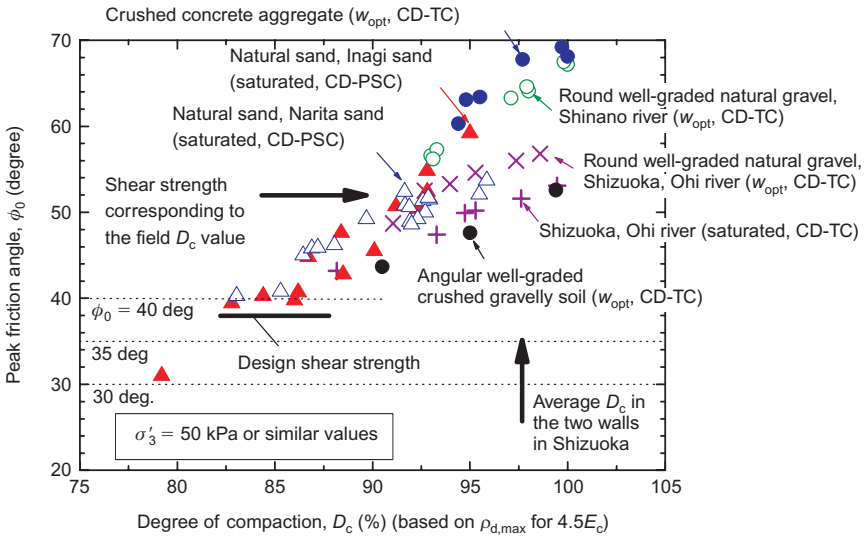

Figure 26. Summary of ϕ_0–D_c (for 4.5 Ec) relations from drained TC and PSC tests at typical operated confining pressures in the field (mostly around 20–50 kPa); the specimens were compacted at w_{opt} (modified from Hirakawa *et al.* 2008; Kiyota *et al.* 2009): Note: w_{opt} in the parenthesis indicates that the specimens when tested were moist as compacted; the others: the specimens when tested were saturated

means that, even when fully saturated, the actual drained shear strength of the backfill was substantially higher than the design value. When correcting the CD TC strength for differences in the grading curve between the gravelly soil used in the CD TC tests and the one used in the field and also when using plane strain shear strength in the design, the difference becomes larger. This analysis indicates that, without losing a sufficient margin for the safety factors against ultimate failure and serviceability limit, we can reduce the conservatism with GRS retaining walls having well-compacted backfill by using a more realistic design shear strength that is higher than the standard design shear strength which is usually used in ordinary design practice.

The second way is to increase the design tensile rupture strength of a given type of polymeric reinforcement, for example, by not using a creep reduction factor, as suggested by Tatsuoka *et al.* (2004, 2006), Tatsuoka (2008) and Kongkitkul *et al.* (2007d). It seems that, in the design for static loading conditions, it would be prudent to employ either of the two methods above, not both, at the current stage of this technology. On the other hand, both methods are employed in the seismic design of soil structures including GRS-RWs for railway structures in Japan (RTRI, 1999, 2007).

The observed geogrid strains and the estimated geogrid forces indicate that it was rather relevant to assume at the design stage of these two walls that the tensile forces in the geogrid layers would be kept constant after the end of wall construction until the end of the prescribed life time. This is also because, at the design stage, it was not possible to predict the manner in which the tensile force would change with time at different locations in different geogrid layers. It seems that the manner in which the tensile force in the geogrid in a given full-scale GRS structure changes with time after the end of wall construction depends on the operated safety factor against the ultimate tensile rupture of the geogrid as well as the operated safety factor against the ultimate failure of the GRS structures and how these safety factors change with time. It is likely that generally the geogrid strain tends to decrease with time when these safety factors are kept high or become higher with time or both. In these cases, the assumption of constant geogrid force during service by the end of the prescribed life time is conservative. When the conservatism in the current design method is reduced (as discussed above), care should be taken to ensure whether the assumption of constant geogrid force during service is reasonably conservative. More research on this issue is needed.

8. CONCLUSIONS

The following conclusions can be derived from the performance of two high geosynthetic-reinforced soil (GRS) walls constructed as part of airport structures and their analyses presented in this paper.

1. Two high GRS walls constructed of highly compacted well-graded gravelly soil, while providing an effective drainage system exhibited very small deformation during construction and negligible residual deformation after the end of wall construction.
2. Corresponding to the above, the increase in the geogrid strain after the end of wall construction was generally very small, or even a decrease was observed, in six monitored geogrid layers in the two walls.
3. The estimated geogrid tensile force based on the time histories of measured geogrid strain by a nonlinear three-component elasto-viscoplastic model either increased at a very small rate, or even decreased with time. It was estimated that, even when the geogrid tensile force tended to continuously increase with time, it would be kept to values that were substantially lower than the respective design ultimate tensile strengths by the end of a typical design life, equal to 50 years.

4. Summarising the above, the possibility of excessive tensile deformation and tensile creep rupture of the geogrid by the end of a design life equal to 50 years is extremely low in these two walls. The analysis presented in this paper suggests that this estimate is also relevant when the lifetime is 100 years.

The current design of geosynthetic reinforcement is based on the force that may be activated in the reinforcement, whereas only strains in the reinforcement arranged in GRS structures can be measured. Therefore, it is very necessary to develop a relevant methodology so that time histories of the force developed in polymeric reinforcement can be estimated from measured time histories of strain for any arbitrary loading history. The methodology described in this paper, which was developed to this end, can be applied to other cases in which time histories of polymeric reinforcement strain are available and relevant laboratory tensile tests to determine the model parameters can be performed.

APPENDIX A: NON-LINEAR THREE-COMPONENT MODEL FOR GEOSYNTHETIC REINFORCEMENT

According to Hirakawa *et al.* (2003) and Kongkitkul *et al.* (2004, 2007a), the current value of the viscous tensile load T^{v} (when the irreversible strain is equal to $\varepsilon^{\mathrm{ir}}$) is obtained as:

$$[T^{\mathrm{v}}]_{(\varepsilon^{\mathrm{ir}})} = \theta(\varepsilon^{\mathrm{ir}}) \cdot [(T^{\mathrm{v}})_{\mathrm{iso}}]_{(\varepsilon^{\mathrm{ir}})} + [1 - \theta(\varepsilon^{\mathrm{ir}})] \cdot [(T^{\mathrm{v}})_{\mathrm{TESRA}}]_{(\varepsilon^{\mathrm{ir}})} \quad \text{(A1-a)}$$

where:

$$[(T^{\mathrm{v}})_{\mathrm{iso}}]_{(\varepsilon^{\mathrm{ir}})} = [T^{\mathrm{f}}(\varepsilon^{\mathrm{ir}}) \cdot g_{\mathrm{v}}(\dot{\varepsilon}^{\mathrm{ir}})]_{(\varepsilon^{\mathrm{ir}})} \quad \text{(A1-b)}$$

$$[(T^{\mathrm{v}})_{\mathrm{TESRA}}]_{(\varepsilon^{\mathrm{ir}})} = \int_{\tau=\varepsilon_1^{\mathrm{ir}}}^{\varepsilon^{\mathrm{ir}}} [\mathrm{d}(T^{\mathrm{v}})_{\mathrm{iso}}]_{(\tau)} \cdot [r_1(\varepsilon^{\mathrm{ir}})]^{\varepsilon^{\mathrm{ir}}-\tau} \quad \text{(A1-c)}$$

where: $\varepsilon_1^{\mathrm{ir}}$ is the value of $\varepsilon^{\mathrm{ir}}$ at the start of integration in Equation A1-c, which is 0.0 in this study. $\theta(\varepsilon^{\mathrm{ir}})$ in Equation A1-a is the viscosity type parameter, which may decrease with $\varepsilon^{\mathrm{ir}}$. The term $r_1(\varepsilon^{\mathrm{ir}})$ in Equation A1-c is the decay function, which may also decrease with $\varepsilon^{\mathrm{ir}}$. Hirakawa *et al.* (2003) reported that geogrid made of Aramid fibre, similar to the one used in this study, exhibited Isotach viscous behaviour from the start of tensile loading where $T = 0$ and $\varepsilon^{\mathrm{ir}} = 0$ until the rupture of the geogrid. Therefore, $\theta = 1.0$ was used and treated unchanged with changes in the $\varepsilon^{\mathrm{ir}}$ value. Then, $[T^{\mathrm{v}}]_{(\varepsilon^{\mathrm{ir}})}$ (Equation A1-a) becomes the same as $[(T^{\mathrm{v}})_{\mathrm{iso}}]_{(\varepsilon^{\mathrm{ir}})}$ (Equation A1-b).

The term $g_{\mathrm{v}}(\dot{\varepsilon}^{\mathrm{ir}})$ in Equation A1-b is the viscosity function, for which the following non-linear function has been proposed for geomaterials (Di Benedetto *et al.* 2002; Tatsuoka *et al.* 2002, 2008; Kongkitkul *et al.* 2008c):

$$g_{\mathrm{v}}(\dot{\varepsilon}^{\mathrm{ir}}) = \alpha \cdot [1 - \exp\{1 - (\frac{|\dot{\varepsilon}^{\mathrm{ir}}|}{\dot{\varepsilon}_{\mathrm{r}}^{\mathrm{ir}}} + 1)^m\}] \ (\geqslant 0) \quad \text{(A2-a)}$$

where α, m and $\dot{\varepsilon}_{\mathrm{r}}^{\mathrm{ir}}$ are constants controlling the quantity of T^{v} for a given $\dot{\varepsilon}^{\mathrm{ir}}$ and T^{f}. On the other hand, Di Benedetto *et al.* (1999, 2005) proposed the following function for $g_{\mathrm{v}}(\dot{\varepsilon}^{\mathrm{ir}})$:

$$g_{\mathrm{v}}(\dot{\varepsilon}^{\mathrm{ir}}) = \alpha^* \cdot \left(|\dot{\varepsilon}^{\mathrm{ir}}|/\dot{\varepsilon}_0^{\mathrm{ir}}\right)^{1+b^*} \quad \text{(A2-b)}$$

where α^*, b and $\dot{\varepsilon}_0^{\mathrm{ir}}$ are constants. Kongkitkul *et al.* (2007a) proposed to combine Equations A2-a and A2-b such that Equation A2-a is activated when the encountered strain rate is high and Equation A2-b when the strain rate is low. They used the combined viscosity function in the simulations of in-air tensile loading tests on geosynthetic reinforcement, in which sustained loading tests were performed for 30 days during otherwise ML at a constant strain rate of 1.0 %/min and the encountered strain rates spanned from high values to extremely low values. As the absolute values of strain rate encountered in this study spanned from low values to very low values, the viscosity function $g_{\mathrm{v}}(\dot{\varepsilon}^{\mathrm{ir}})$ having the form of Equation A2-b is appropriate. By back-analysis of the test results on Aramid fibre that were determined for short-term creep behaviour (Hirakawa *et al.* 2003), $\alpha^* = 0.18$, $b^* = -0.65$ and $\dot{\varepsilon}_0^{\mathrm{ir}} = 10^{-6}$ %/s were found relevant. These parameters were re-confirmed by successful simulations of the tensile load–strain relations as well as time histories of creep strain obtained by another series of in-air tensile loading tests presented in this study (Figures 10(a) and (b)).

APPENDIX B: SIMULATION UNDER UNLOADING CONDITION

B1. Reference load–strain relation during unloading

Geosynthetic reinforcement exhibits usually substantially different shapes of tensile load–strain curves during primary loading and unloading. Then, it becomes necessary to introduce imaginary primary loading and imaginary primary unloading curves, $T^{\mathrm{f}} = g(\varepsilon^{\mathrm{ir}})$ and $T^{\mathrm{f}} = -g(-\varepsilon^{\mathrm{ir}})$, having a shape that is similar to the shape of actual unloading curve, as illustrated in Figure 27 (Kongkitkul *et al.* 2004). The shape of these imaginary functions is substantially different from the shape of the actual primary loading curve, $T^{\mathrm{f}} = f(\varepsilon^{\mathrm{ir}})$. Unloading and reloading curves from any arbitrary state are obtained by scaling these imaginary functions. Two polynomial functions were respectively determined for $T^{\mathrm{f}} = f(\varepsilon^{\mathrm{ir}})$ and $T^{\mathrm{f}} = g(\varepsilon^{\mathrm{ir}})$ by best fitting of the inferred inviscid tensile load–irreversible strain curves (at zero irreversible strain rate) during primary loading and unloading.

The tensile load–strain relations during unloading illustrated in Figure 27 are obtained as follows.

1. During the first primary loading from the origin ***o*** ($\varepsilon_{\mathrm{o}}^{\mathrm{ir}} = 0$, $T_{\mathrm{o}}^{\mathrm{f}} = 0$) until point ***a***, the tensile load–

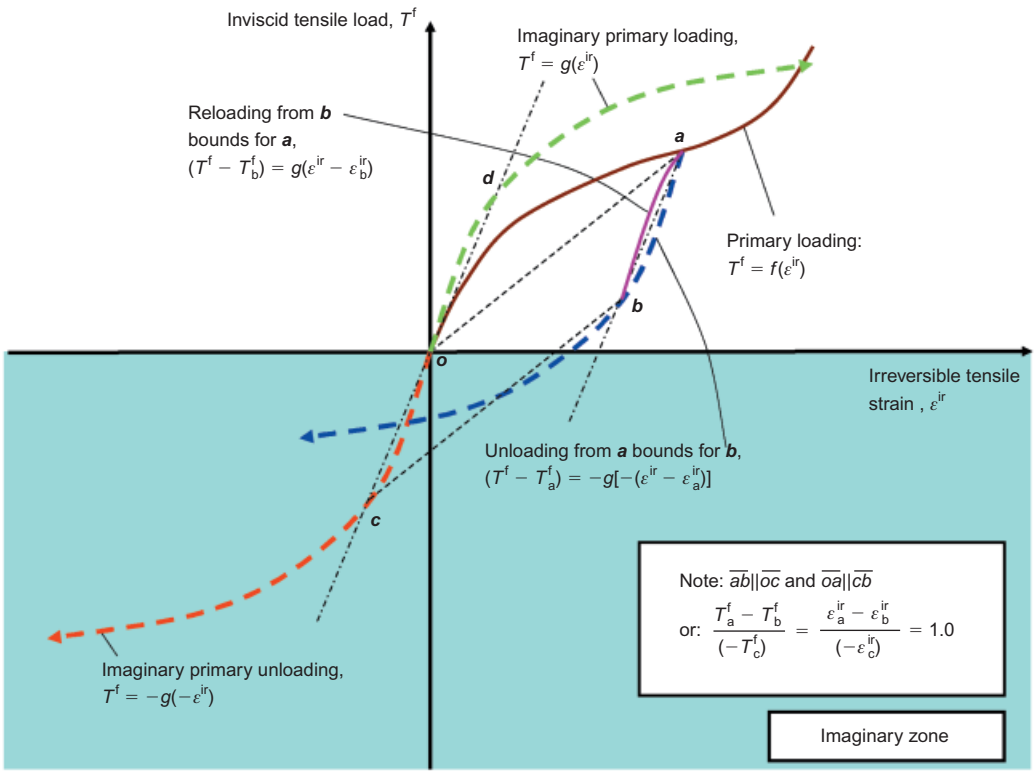

Figure 27. Implementation of different functions to simulate the tensile load–strain relations during unloading (after Kongkitkul *et al.* 2004)

strain curve follows the primary loading curve, $T^f = f(\varepsilon^{ir})$.

2. Suppose that loading is reversed at point ***a***. The unloading curve is obtained by using the known imaginary primary unloading curve $T^f = -g(-\varepsilon^{ir})$ and the coordinate at point ***a***, $(\varepsilon^{ir}_a, T^f_a)$, as:

$$\left(T^f - T^f_a\right) = -g\left[-\left(\varepsilon^{ir} - \varepsilon^{ir}_a\right)\right] \tag{B1-a}$$

$$\frac{T^f_a - T^f_b}{-\left(T^f_c\right)} = \frac{\varepsilon^{ir}_a - \varepsilon^{ir}_b}{-\left(\varepsilon^{ir}_c\right)} = 1.0 \tag{B1-b}$$

where point ***c*** $(\varepsilon^{ir}_c, T^f_c)$ is the intersection of 'the straight line from the origin ***o*** which is parallel to the straight line between points ***a*** and ***b*** with the imaginary primary unloading curve $T^f = -g(-\varepsilon^{ir})$.

B2. Isotach-type viscous load component during unloading

The isotach-type viscous load component, $(T^v)_{iso}$, is positive during primary loading with positive $\dot{\varepsilon}^{ir}$ and negative during unloading with negative $\dot{\varepsilon}^{ir}$. It is natural to assume that the viscous load component, T^v, is zero at the start of unloading. For these reasons, it was assumed that the value of $(T^v)_{iso}$ during unloading condition is given as:

$$(T^v)_{iso} = T^{f*} \cdot g_v(\dot{\varepsilon}^{ir}) \tag{B2}$$

where T^{f*} is the inviscid load component used only to obtain the viscous load component and is obtained as follows. For the value of $(T^v)_{iso}$ at point ***b*** during unloading (Figure 28), T^{f*} is the value of T^f at point ***b**** along the imaginary primary unloading curve that corresponds to point ***b***, obtained as:

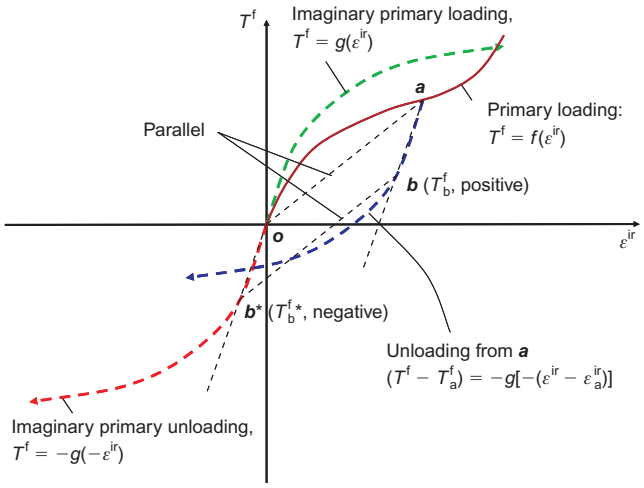

Figure 28. Method to obtain the viscous load component unloading (after Kongkitkul *et al.* 2004)

$$T^{f*} = T^f_b - T^f_a \ (\leqslant 0) \tag{B3}$$

Therefore, in this case, T^{f*} is negative. Consequently, $(T^v)_{iso}$ during unloading is negative as the result of $g_v(\dot{\varepsilon}^{ir})$ is always positive, irrespective of the signs of $\dot{\varepsilon}^{ir}$.

NOTATIONS

Basic SI units are given in parentheses.

A_1, A_2 constants of an exponential equation for geogrid strain (dimensionless)

g_v viscosity function of a non-linear three-component model (dimensionless)
h_s loading history parameter (dimensionless)
b^* parameter of viscosity function (dimensionless)
c parameter of decay function (dimensionless)
c_θ parameter of viscosity type function (dimensionless)
D_c degree of compaction of the backfill
f inviscid tensile load–strain relation during primary loading (dimensionless)
g inviscid tensile load–strain relation during unloading (dimensionless)
m parameter of viscosity function (dimensionless)
T tensile load or force (N/m)
T^f inviscid tensile load of the non-linear three-component model (N/m)
T^{f*} inviscid tensile load used to obtain viscous tensile load during unloading (N/m)
T^v viscous tensile load of the non-linear three-component model (N/m)
$(T^v)_{iso}$ Isotach-type viscous tensile load of the non-linear three-component model (N/m)
$(T^v)_{TESRA}$ TESRA-type viscous tensile load of the non-linear three-component model (N/m)
r_1 decay function of non-linear three-component model (dimensionless)
r_i parameter of decay function (dimensionless)
r_f parameter of decay function (dimensionless)
t_1 constant of an exponential equation for geogrid strain (dimensionless)
t_2 constant of an exponential equation for geogrid strain (dimensionless)
Δt elapsed time after the end of wall construction (s)
α parameter of viscosity function (dimensionless)
α^* parameter of viscosity function (dimensionless)
ε tensile strain of geogrid (dimensionless)
ε_{ir} irreversible tensile strain of geogrid (dimensionless)
ε_1^{ir} irreversible tensile strain at the start of integration (dimensionless)
ε_{r1}^{ir} parameter of decay function (dimensionless)
ε_θ^{ir} parameter of viscosity type function (dimensionless)
$\dot{\varepsilon}$ tensile strain rate (s^{-1})
$\dot{\varepsilon}^e$ elastic strain rate (s^{-1})
$\dot{\varepsilon}^{ir}$ irreversible strain rate (s^{-1})
$\dot{\varepsilon}_r^{ir}$ parameter of viscosity function (s^{-1})
$\dot{\varepsilon}_0^{ir}$ parameter of viscosity function (s^{-1})
$\Delta\varepsilon$ tensile strain increment of geogrid after the end of wall construction (dimensionless)
θ viscosity type function (dimensionless)
θ_{ini} parameter of viscosity type function (dimensionless)
θ_{end} parameter of viscosity type function (dimensionless)
ϕ_o angle of internal friction to the origin (°)

ABBREVIATIONS

CD consolidated drained
GRS geosynthetic-reinforced soil
HDPE high-density polyethylene
ML monotonic loading
PSC plane strain compression
TC triaxial compression

REFERENCES

Allen, T. M. & Bathurst, R. J. (2002a). Soil reinforcement loads in geosynthetic walls at working stress conditions. *Geosynthetics International*, **9**, Nos. 5–6, 525–566.

Allen, T. M. & Bathurst, R.J. (2002b). Observed long-term performance of geosynthetic walls and implications for design. *Geosynthetics International*, **9**, Nos. 5–6, 567–606.

Bathurst, R. J., Allen, T. M. & Walters, D. L. (2002). Short-term strain and deformation behavior of geosynthetic walls at working stress conditions. *Geosynthetics International*, 9, Nos. 5–6, 451–482.

Bussert, F. & Naciri, O. (2009). Experiences from deformation measurements on geosynthetic reinforced retaining walls. *Proceedings of the 4th European Geosynthetics Conference (EuroGeo 4)*, Edinburgh, International Geosynthetics Society, Nottinghamshire, UK, paper No. 88 (CD).

Di Benedetto, H., Sauzéat, C. & Geoffroy, H. (1999). Modelling viscous effects for sand and behaviour in the small strain domain. *Proceeding of the 2nd International Symposium on Pre-failure Deformation Characteristics of Geomaterials*, IS Torino, Balkema, Rotterdam, The Netherlands, Vol. 2, pp. 1357–1367.

Di Benedetto, H., Tatsuoka, F. & Ishihara, M. (2002). Time-dependent shear deformation characteristics of sand and their constitutive modelling. *Soils and Foundations*, **42**, No. 2, 1–22.

Di Benedetto, H., Tatsuoka, F., Lo Presti, D., Sauzéat, C. & Geoffroy, H. (2005). Time effects on the behaviour of geomaterials. Keynote lecture, *Proceedings of the 3rd International Symposium on Deformation Characteristics of Geomaterials*, IS Lyon '03, Di Benedetto, H., Doanh, T., Geoffroy, H. & Sauzeat, C. Editors, September, 2003, Taylor and Francis, London, Vol. 2, pp. 59–123.

Fujinami, T., Sugimoto, T., Nakamura, Y., Kawahata, S., Funada, H., Yoshida, T., Ito, M. & Yoshida, N. (2007). Application of reinforced soil wall to high embankment in Mt. Fuji Shizuoka Airport, Part III: Field observation. *Proceeding of the 42nd Japan National Conference on Geotechnical Engineering*, Nagoya, Japanese Geotechnical Society, Tokyo, Japan, No. 804, pp.1603–1604 (in Japanese).

Fujinami, T., Sugimoto, T., Yamashita, D. & Kawahata, S. (2009). Application of geosynthetic-reinforced wall technology and backfill compaction control in constructing high embankment for Mt. Fuji Shizuoka Airport. *Monthly Journal Kiso-ko (Foundation Engineering and Equipment)*, **37**, No. 7, 92–95 (in Japanese).

Fujita, Y., Sugimoto, T., Koha, T. & Tsuda, M. (2007). Application of reinforced soil wall to high embankment in Mt. Fuji Shizuoka Airport, Part I: Design and planning. *Proceeding of the 42nd Japan National Conference on Geotechnical Engineering*, Nagoya, Japanese Geotechnical Society, Tokyo, Japan, No. 802, pp. 1599–1600 (in Japanese).

Fujita, Y., Sugimoto, T., Tsuda, M., Nakamura, Y., Kawahata, S., Funada, H., Yoshida, T., Ito, M. & Yoshida, K. (2008). High geogrid-reinforced retaining walls for a new airport. *Proceedings of the 4th Asian Regional Conference on Geosynthetics (GeoAsia 2008)*,

Shanghai, China, 17–20 June 2008, Li, G., Chen, Y. & Tang, X., Editors, Zhejiang University Press, Hangzhou, China & Springer, Berlin, Germany, pp. 645–650.

Hirakawa, D., Kongkitkul, W., Tatsuoka, F. & Uchimura, T. (2003). Time-dependent stress-strain behaviour due to viscous properties of geogrid reinforcement. *Geosynthetics International*, **10**, No. 6, 176–199.

Hirakawa, D., Kawaharazono, M. & Tatsuoka, F. (2008). Effect of compaction conditions on strength and deformation characteristics of backfill materials. *Journal of Japanese Society for Civil Engineers*, **C-64**, No. 2, 253–266 (in Japanese).

Kiyota, T., Hara, D., Seida, K., Mochizuki, K., Mochizuki, K., Nagai,Y. & Tatsuoka, F. (2009). Effects of the degree of compaction on the deformation and strength characteristics of sands and gravels. *Monthly Journal Kiso-ko (Foundation Engineering and Equipment)*, **37**, No. 7 (July), 27–31 (in Japanese).

Kongkitkul, W. & Tatsuoka, F. (2007). A theoretical framework to analyse the behaviour of polymer geosynthetic reinforcement in temperature-accelerated creep tests. *Geosynthetics International*, **14**, No. 1, 23–38.

Kongkitkul, W., Hirakawa, D., Tatsuoka, F. & Uchimura, T. (2004). Viscous deformation of geosynthetic reinforcement under cyclic loading conditions and its model simulation. *Geosynthetics International*, **11**, No. 2, 73–99.

Kongkitkul, W., Hirakawa, D. & Tatsuoka, F. (2007a). Viscous behaviour of geogrids; experiment and simulation. *Soils and Foundations*, **47**, No. 2, 265–283.

Kongkitkul, W., Tatsuoka, F. & Hirakawa, D. (2007b). Effects of reinforcement type and loading history on the deformation of reinforced sand in plane strain compression. *Soils and Foundations*, **47**, No. 2, 395–414.

Kongkitkul, W., Tatsuoka, F. & Hirakawa, D. (2007c). Rate-dependent load-strain behaviour of geogrid arranged in sand under plane strain compression. *Soils and Foundations*, , **47**, No. 3, 473–491.

Kongkitkul, W., Tatsuoka, F. & Hirakawa, D. (2007d). Creep rupture curve for simultaneous creep deformation and degradation of geosynthetic reinforcement. *Geosynthetics International*, **14**, No. 4, 189–200.

Kongkitkul, W., Hirakawa, D., Tatsuoka, F. & Kanemaru, T. (2007e). Effects of geosynthetic reinforcement type on the strength and stiffness of reinforced sand in plane strain compression. *Soils and Foundations*, **47**, No. 6, 1109–1122.

Kongkitkul, W., Hirakawa, D. & Tatsuoka, F. (2008a). Residual deformation of geosynthetic-reinforced sand in plane strain compression affected by viscous properties of geosynthetic reinforcement. *Soils and Foundations*, **48**, No. 3, 333–352.

Kongkitkul, W., Hirakawa, D., Sugimoto, T., Kawahata, S., Yoshida, T., Ito, S. & Tatsuoka, F. (2008b). Post-construction time history of tensile load in geogrid arranged in a full-scale high wall. *Proceedings of the 4th Asian Regional Conference on Geosynthetics (GeoAsia 2008)*, Shanghai, China, 17–20 June 2008, Li, G., Chen, Y. & Tang, X., Editors, Zhejiang University Press, Hangzhou, China & Springer, Berlin, Germany, pp. 64–69.

Kongkitkul, W., Tatsuoka, F., Duttine, A., Kawabe, S., Enomoto, T. & Di Benedetto, H. (2008c). Modelling and simulation of rate-dependent stress-strain behaviour of granular materials in shear. *Soils and Foundations*, **48**, No. 2, 175–194.

Koseki, J., Bathurst, R. J., Güler, E., Kuwano, J. & Maugeri, M. (2006). Seismic stability of reinforced soil walls. Keynote Lecture, *Proceedings of the 8th International Conference on Geosynthetics*, Kuwano, J. & Koseki, J., Editors, Yokohama, Japan, Millpress, Rotterdam, The Netherlands, Vol. 1, pp. 51–77.

Latha, G. M. & Krishna, A. M. (2008). Seismic response of reinforced soil retaining wall models: Influence of backfill relative density. *Geotextiles and Geomembranes*, **26**, No. 4, 335–349.

RTRI (1999). *Seismic Design Standard for Railway Structures*. Railway Technical Research Institute (RTRI), Maruzen Tokyo, Japan (in Japanese)

RTRI (2007). *Design Standard for Railways Earth Structures*. Railway Technical Research Institute (RTRI), Maruzen Tokyo, Japan (in Japanese).

Takagi, H., Sugimoto, T., Nakamura, Y., Kawahata, S., Funada, H., Yoshida, T., Ito, S. & Tatta, N. (2007). Application of reinforced soil wall to high embankment in Mt. Fuji Shizuoka Airport, Part II: Earthwork. *Proceedings of the 42nd Japan National Conference on Geotechnical Engineering*, Nagoya, Japanese Geotechnical Society, Tokyo, Japan, No. 803, pp. 1601–1602 (in Japanese).

Tatsuoka, F. (2008). Geosynthetics engineering, combining two engineering disciplines. Keynote Lecture, *Proceedings of the 4th Asian Regional Conference on Geosynthetics (GeoAsia 2008)*, Shanghai, China, 17–20 June 2008, Li, G., Chen, Y. & Tang, X., Editors, Zhejiang University Press, Hangzhou, China & Springer, Berlin, Germany, Vol. 2, pp. 1–35.

Tatsuoka, F. (2009). Design shear strength and compaction control of backfill – a current wide and deep gap between Industry and Academia. Panel discussions for Industry and Academia Session, *Proceedings of the 13th Asian Regional Conference on Soil Mechanics and Geotechnical Engineering*, Kolkata, 10–14 December 2007, Vol. 2.

Tatsuoka, F., Tateyama, M., Uchimura, T. & Koseki, J. (1997). Geosynthetics reinforced soil retaining walls as important permanent structures, 1996–1997 Mercer Lecture. *Geosynthetics International*, **4**, No. 2, 81–136.

Tatsuoka, F., Koseki, J., Tateyama, M., Munaf, Y. & Horii, N. (1998). Seismic stability against high seismic loads of geosynthetic-reinforced soil retaining structures. Keynote Lecture, *Proceedings of the 6th International Conference on Geosynthetics*, Atlanta, Industrial Fabrics Association International, St Paul, MN, USA, Vol. 1, pp. 103–142.

Tatsuoka, F., Ishihara, M., Di Benedetto, H. & Kuwano, R. (2002). Time-dependent shear deformation characteristics of geomaterials and their simulation. *Soils and Foundations*, **42**, No. 2, 103–129.

Tatsuoka, F., Hirakawa, D., Shinoda, M., Kongkitkul, W. & Uchimura,T. (2004). An old but new issue; viscous properties of polymer geosynthetic reinforcement and geosynthetic-reinforced soil structures. Keynote Lecture, *Proceedings of the 3rd Asian Regional Conference on Geosynthetics (GeoAsia 2004)*, Shim, J. B., Yoo, C. & Jeon, H.-Y., Editors, Seoul, pp. 29–77.

Tatsuoka, F., Kongkitkul, W. & Hirakawa, D. (2006). Viscous property and time-dependent degradation of geosynthetic reinforcement. *Proceedings of the 8th International Conference on Geosynthetics*, Kuwano, J. & Koseki, J., Editors, Yokohama, Japan, Vol. 4, pp. 1587–1590.

Tatsuoka, F., Tateyama, M., Mohri, Y. & Matsushima, K. (2007). Remedial treatment of soil structures using geosynthetic-reinforcing technology. *Geotextiles and Geomembranes*, **25**, Nos. 4–5, pp. 204–220.

Tatsuoka, F., Di Benedetto, H., Enomoto, T., Kawabe, S. & Kongkitkul, W. (2008). Various viscosity types of geomaterials in shear and their mathematical expression. *Soils and Foundations*, **48**, No. 1, 41–60.

Walters, D. L., Allen, T. M. & Bathurst, R. J. (2002). Conversion of geosynthetic strain to load using reinforcement stiffness. *Geosynthetics International*, **9**, Nos. 5–6, 483–523.

The Editor welcomes discussion on all papers published in Geosynthetics International. Please email your contribution to discussion@geosynthetics-international.com by 15 August 2010.